J. Fluid Mech. (2017), *vol.* 815, *pp.* 169–198.
doi:10.1017/jfm.2017.36

Local versus volume-integrated turbulence and mixing in breaking internal waves on slopes

Robert S. Arthur[1,2,†], Jeffrey R. Koseff[2] and Oliver B. Fringer[2]

[1]Department of Civil and Environmental Engineering, University of California, Berkeley, CA 94720, USA

[2]The Bob and Norma Street Environmental Fluid Mechanics Laboratory, Department of Civil and Environmental Engineering, Stanford University, Stanford, CA 94305, USA

(Received 13 October 2015; revised 12 January 2017; accepted 12 January 2017)

Using direct numerical simulations (DNS), we explore local and volume-integrated measures of turbulence and mixing in breaking internal waves on slopes. We consider eight breaking wave cases with a range of normalized pycnocline thicknesses $k\delta$, where k is the horizontal wavenumber and δ is the pycnocline thickness, but with similar incoming wave properties. The energetics of wave breaking is quantified in terms of local turbulent dissipation and irreversible mixing using the method of Scotti & White (*J. Fluid Mech.*, vol. 740, 2014, pp. 114–135). Local turbulent mixing efficiencies are calculated using the irreversible flux Richardson number R_f^* and are found to be a function of the turbulent Froude number Fr_k. Volume-integrated measures of the turbulent mixing efficiency during wave breaking are also made, and are found to be functions of $k\delta$. The bulk turbulent mixing efficiency ranges from 0.25 to 0.37 and is maximized when $k\delta \approx 1$. In order to connect local and bulk mixing efficiency measures, the variation in the bulk turbulent mixing efficiency with $k\delta$ is related to the turbulent Froude number at which the maximum total mixing occurs over the course of the breaking event, Fr_k^{max}. We find that physically, Fr_k^{max} is controlled by the vertical length scale of billows at the interface during wave breaking.

Key words: internal waves, topographic effects, turbulent mixing

1. Introduction

Breaking internal waves on slopes are of critical oceanographic importance, particularly in quantifying dissipation and mixing in the global ocean energy budget. Munk & Wunsch (1998) suggested that the ocean is primarily mixed by strong turbulent events at boundaries, with the mixed water masses then being exported into the ocean interior. The review of Wunsch & Ferrari (2004) expands on this claim by asking whether breaking internal waves at boundaries can account for the global average mixing in the ocean being 10 times higher than the observed open ocean mixing away from topography. A thorough review of breaking internal waves on the

† Email address for correspondence: barthur@berkeley.edu

continental shelf and slope was made by Lamb (2014), but the relative contribution of breaking internal waves at boundaries to the global ocean energy budget remains poorly understood.

Shoaling and breaking internal waves on slopes are also important drivers of transport and mixing in nearshore ecosystems. A variety of field observations have quantified the effect of breaking internal waves on the nearshore distributions of biologically important scalars. These include temperature (Leichter *et al.* 1996; Davis & Monismith 2011; Walter *et al.* 2012), nutrients (Leichter *et al.* 1996; Omand *et al.* 2011), sediments (Bogucki, Dickey & Redekopp 1997; Klymak & Moum 2003; Hosegood, Bonnin & van Haren 2004; Hosegood & van Haren 2004; Carter, Gregg & Lien 2005; Quaresma *et al.* 2007), larvae (Pineda 1994) and dissolved oxygen (Walter *et al.* 2014*b*).

An understanding of the turbulent energetics of stratified flows is necessary to solve the aforementioned oceanographic problems. The turbulent mixing efficiency is particularly important because it allows mixing rates to be inferred from measurements of dissipation. One can use the mixing efficiency to estimate the eddy diffusivity, $K_\rho = \Gamma\epsilon/N^2$, where Γ is the mixing coefficient, ϵ is the turbulent dissipation and N is the buoyancy frequency (Osborn 1980). Such parameterizations of mixing can also be used in large-scale models that do not resolve small-scale turbulent mixing processes. The mixing efficiency of stratified turbulent flows has traditionally been quantified from the turbulent kinetic energy equation using the flux Richardson number

$$R_f = \frac{\mathcal{B}}{\mathcal{B}+\epsilon}, \tag{1.1}$$

where $\mathcal{B}$ is the turbulent buoyancy flux (e.g. Osborn 1980; Ivey & Imberger 1991; Shih *et al.* 2005). The mixing coefficient is related to the flux Richardson number as

$$\Gamma = \frac{R_f}{1-R_f} = \frac{\mathcal{B}}{\epsilon}. \tag{1.2}$$

Assuming steady, homogeneous turbulence (a balance of turbulent production with the buoyancy flux and dissipation), Osborn (1980) suggested a critical flux Richardson number $R_f^{crit} \approx 0.17$, which gives $\Gamma \approx 0.2$. Based on the relationship between R_f and Γ in (1.2), both of these quantities are often referred to as the 'mixing efficiency' in the literature. In this paper, we refer to the mixing efficiency as R_f.

As reviewed by Ivey, Winters & Koseff (2008), many field studies have examined the mixing efficiency from turbulence measurements in the ocean, finding a range of values for different conditions. These studies use measurements of fine-scale velocity and temperature gradients to quantify the dissipation of turbulent kinetic energy ϵ and the dissipation of scalar variance χ, respectively. For example, Oakey (1982) found $\Gamma \approx 0.24$ using microstructure profiles of the upper ocean (50–100 m depth), while Yamazaki & Osborn (1993) found $R_f \approx 0.05$ using a submarine-mounted instrument in a turbulent shear layer. Additionally, using microstructure profiles, Seim & Gregg (1995) estimated $R_f = 0.22 \pm 0.1$ for a shear instability event, Gargett & Moum (1995) estimated $R_f \approx 0.4$ in a turbulent tidal front and Moum (1996) estimated $R_f = 0.13$–0.17 in turbulent patches in the main ocean thermocline. Several studies have also inferred how R_f varies when different parameterizations are used (e.g. Dunckley *et al.* 2012; Bluteau, Jones & Ivey 2013). The advent of moored turbulence measurements has allowed for the collection of turbulence data over longer time series. Several studies, such as Davis & Monismith (2011) and Walter

et al. (2014*a*), have used moored instruments to estimate the mixing efficiency during breaking internal wave events on slopes. While it is clear from these studies that the mixing efficiency depends upon the state of the turbulence that is driving mixing, the intermittent (in time) and patchy (in space) nature of ocean turbulence makes a complete observational understanding of the mixing efficiency difficult.

For this reason, many studies have turned to more idealized laboratory and numerical set-ups to quantify the mixing efficiency of stratified turbulent flows. Using laboratory experiments, Ivey & Imberger (1991) extended the definition of the flux Richardson number to include the entire turbulent kinetic energy budget such that $R_f = \mathcal{B}/m$, where m is the net mechanical energy available to sustain turbulent motions (including production, advection and transport). They then characterized R_f in terms of the turbulent Reynolds number $Re_T = uL_C/\nu$ and the turbulent Froude number $Fr_T = u/NL_C$, where L_C is the centred displacement scale, a measure of observed turbulent overturns, and $u \sim (\epsilon L_C)^{1/3}$ is the turbulent velocity scale. For large enough turbulent Reynolds numbers to sustain turbulence ($Re_T > 15$), they found that R_f is maximized for $Fr_T \approx 1$. For $Fr_T < 1$, turbulent mixing is suppressed by buoyancy, while for $Fr_T > 1$, turbulent mixing is reduced because the stratification is weak. Both Davis & Monismith (2011) and Walter *et al.* (2014*a*) found good agreement with Ivey & Imberger (1991) using data from field observations of breaking internal waves on slopes, noting the potential effect of the advection of turbulent kinetic energy on the measured mixing efficiency in these events.

Using direct numerical simulations (DNS), Shih *et al.* (2005) presented another parameterization of R_f in terms of the buoyancy Reynolds number or turbulence activity number $Re_b = \epsilon/\nu N^2$. They found that for $Re_b < 7$ (the 'diffusive' regime), R_f is scattered and often negative due to countergradient turbulent buoyancy fluxes, ranging from -0.4 to 0.2. For $7 < Re_b < 100$ (the 'intermediate regime'), R_f is fairly constant around 0.2, slightly larger than the critical value of Osborn (1980). For $Re_b > 100$ (the 'energetic' regime), R_f declines as Re_b increases ($R_f = \alpha\, Re_b^{-1/2}$, $\alpha = 1.5$) because the turbulence is actively growing. Several studies have extended the analysis of Shih *et al.* (2005) to larger values of Re_b, which are common in the field but infeasible in DNS. Both Davis & Monismith (2011) and Walter *et al.* (2014*a*) found a similar power-law relationship between R_f and Re_b in the energetic regime, with $\alpha = 4.5$ and $\alpha = 2$, respectively. A direct comparison between the results of Shih *et al.* (2005), Davis & Monismith (2011) and Walter *et al.* (2014*a*) is presented in Walter *et al.* (2014*a*), see figure 12 therein. It should be noted that the coefficient α is not universally $O(1)$. A study of stratified turbulence in the atmospheric boundary layer by Lozovatsky & Fernando (2013) again found $R_f = \alpha Re_b^{-1/2}$ scaling, but with $\alpha = 50$. Mater & Venayagamoorthy (2014) have since reconsidered the results of Shih *et al.* (2005) in terms of a shear strength parameter $ST_L = Sk/\epsilon$, a turbulent Froude number $Fr_k = \epsilon/Nk$ and a turbulent Reynolds number $Re_L = k^2/\nu\epsilon$, where S is the mean shear and k is the turbulent kinetic energy. Using this framework, they discussed the potential ambiguities of using single parameters such as Re_b and the gradient Richardson number $Ri_g = N^2/S^2$ to characterize the mixing efficiency.

The mixing efficiency of stratified turbulent flows can also be quantified by separating the potential energy into its available and background components (Winters *et al.* 1995). The background potential energy represents the lowest possible potential energy state of a system if it were to be adiabatically rearranged, and is obtained numerically by sorting the density field. The available potential energy, then, is the difference between the total potential energy and the background, and is available for exchange with the kinetic energy. Changes in the background potential energy

can only occur due to molecular diffusion, and therefore represent a true measure of irreversible mixing. Reversible turbulent 'stirring' is contained in the available potential energy field. Winters *et al.* (1995) used these definitions to define a volume-integrated measure of the mixing efficiency. Several studies have employed this method to quantify the energetics of stratified shear flows. Smyth, Moum & Caldwell (2001) used DNS to compare mixing efficiency values calculated with the Winters *et al.* (1995) method to a typical approximation used in the field, the Osborn–Cox model (Osborn & Cox 1972), which is based on the dissipation of scalar variance χ. Peltier & Caulfield (2003) also used the Winters *et al.* (1995) method to relate a cumulative measure of the mixing efficiency to the initial Richardson number Ri_0.

Much of the laboratory and numerical work examining the mixing efficiency of stratified turbulent flows has focused directly on breaking internal wave events. For example, Michallet & Ivey (1999) and Boegman, Ivey & Imberger (2005) calculated the bulk mixing efficiency of breaking internal wave events on a slope in the laboratory, finding a range of mixing efficiency values between 0.05 and 0.25 for various wave and slope conditions. Their mixing efficiency calculation was based on the total potential energy gain in the system due to the breaking wave event. Additionally, Hult, Troy & Koseff (2011) calculated the mixing efficiency within turbulent patches generated by breaking internal waves propagating over a ridge. However, due to the difficulty of measuring the turbulent buoyancy flux $\mathcal{B}$ in the laboratory, they calculated dissipation and inferred R_f from the parameterizations of Ivey & Imberger (1991) and Shih *et al.* (2005), and found $R_f \approx 0.10 - 0.17$ in the turbulent patch created by wave breaking. Although turbulence existed in the upper and lower density layers during their experiments, it did not contribute to mixing because these layers were unstratified (thus $R_f \approx 0$ there). This resulted in an overall R_f of 0.04–0.07 for the entire domain.

Using numerical simulations, Fringer & Street (2003) employed the method of Winters *et al.* (1995) to calculate the mixing efficiency of breaking progressive internal waves as a function of the non-dimensional pycnocline thickness $k\delta$. They found an average bulk mixing efficiency of 0.42, with a peak around 0.49 when $k\delta \approx 1$. This corresponds to the most efficient transfer of energy from the large-scale wave to the turbulent scales, where mixing takes place. Finally, Arthur & Fringer (2014) used the method of Winters *et al.* (1995) to quantify the energetics of breaking internal waves on slopes. They calculated the bulk mixing efficiency as a function of the incoming wave amplitude and bathymetric slope, and found a range of values between 0.14 and 0.20.

There are several drawbacks associated with the mixing efficiency measures explained above. First, the flux Richardson number R_f is affected by countergradient turbulent buoyancy fluxes, especially at low Reynolds number Re_b, leading to small and potentially negative values of R_f (Venayagamoorthy & Koseff 2016). Second, the Winters *et al.* (1995) method relies on domain-integrated quantities of dissipation and mixing in order to define the mixing efficiency. Thus, the energetics cannot be broken down into smaller (local) regions of the flow. In order to address both of these issues, Scotti & White (2014) developed a new measure of local turbulent energetics based on a local definition of the rate of change of the background potential energy. Their method builds upon the framework of Winters *et al.* (1995) to provide a measure of irreversible turbulent mixing. This facilitates calculations of local turbulent mixing efficiency that are not affected by countergradient buoyancy fluxes. The method of Scotti & White (2014) has yet to be applied to the problem of breaking internal waves on slopes.

In the present study, we use the method of Scotti & White (2014) to explore local and volume-integrated measures of turbulence and mixing in breaking internal waves on slopes. We focus on the effect of pycnocline thickness on turbulence and mixing, which is relevant in lakes and the coastal ocean, but has not been considered in previous laboratory-scale studies of breaking internal waves on slopes (e.g. Michallet & Ivey 1999; Boegman *et al.* 2005; Arthur & Fringer 2014). We employ DNS to consider eight breaking wave cases with a range of pycnocline thicknesses, but with fixed initial amplitude, and therefore similar incoming wave properties. Section 2 explains our computational approach, which is based on that of Arthur & Fringer (2014) and Arthur & Fringer (2016). Section 3 provides an overview of the breaking process for different pycnocline thicknesses. Then, in §§ 4 and 5, we explore local and volume-integrated turbulent energetics quantities, respectively. Finally, in § 6, we present a connection between local and volume-integrated energetics perspectives.

2. Computational approach

2.1. *Computational set-up*

We perform DNS of breaking internal waves on slopes in an idealized, laboratory-scale domain using the parallel Navier–Stokes code of Cui (1999). This code employs the fractional-step method of Zang, Street & Koseff (1994), and has been used extensively in the past to study geophysical flows at the laboratory scale (see Venayagamoorthy & Fringer 2007; Chou & Fringer 2010; Arthur & Fringer 2014, 2016). The computational set-up used here is based on that of Arthur & Fringer (2014, 2016), and is summarized in figure 1.

Computations are made on an orthogonal curvilinear grid of size $n_1 \times n_2 \times n_3 = 1152 \times 96 \times 128 \approx 14 \times 10^6$ points that was generated using the open-source software gridgen (available online at https://code.google.com/p/gridgen-c/). Grid stretching of the form $\Delta x_i^k = r\Delta x_i^{k+1}$, where r is the stretching factor and k is the index of the grid point, is employed in the horizontal (x_1) and vertical (x_3) directions to increase resolution in the breaking region. Grid spacing in the lateral (x_2) direction is constant. In the horizontal direction, stretching is applied from $x_1 = 0$ to L_s with $r = 1.01$, concentrating 1024 points (approximately 90 % of n_1) into the sloping region. The grid is also stretched slightly in x_1 in the sloping region to maintain orthogonality. In the vertical direction, stretching is performed twice. First, grid points are concentrated toward the bottom with $r = 1.02$ in order to resolve the flow near the wall. Second, 100 of 128 points (78 %) are concentrated in the bottom 35 % of the domain with $r = 1.07$ in order to resolve the pycnocline and lower layer during breaking. The resulting grid resolution at the pycnocline in the breaking region is approximately $\Delta x_1 \times \Delta x_2 \times \Delta x_3 = 4$ mm $\times$ 1 mm $\times$ 2 mm. Near the bottom wall, the vertical coordinate is measured in wall units $x_3^+ = x_3/\delta_S$, where $\delta_S = \sqrt{2\nu/\omega}$ (see § 2.2 for the definition of the wave frequency ω). The vertical resolution near the wall is therefore $\Delta x_3^+ = \Delta x_3/\delta_S < 1$. In the worst case scenario, the grid spacing is found to be within approximately one order of magnitude of the Kolmogorov length scale η_k, providing sufficient resolution for DNS (see Arthur & Fringer 2014). The boundary conditions for all velocity components are no slip on the bottom wall and free slip on the top, left and right walls. The density field has a gradient-free boundary condition on the top, bottom, left and right walls. All variables are periodic in the lateral (x_2) direction.

A time step of $\Delta t = 0.003$ s is used for all simulations. The number of time steps varies by case and ranges from 18 000 for case 1 to for 27 000 for case 8. Simulations were run on the US Army Research Lab Department of Defense Supercomputing

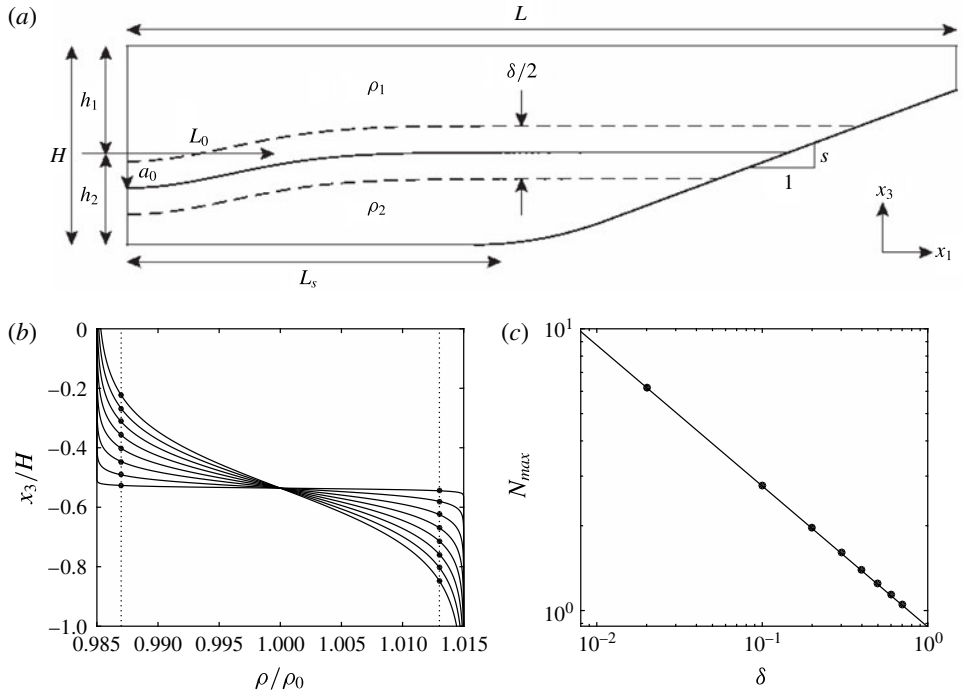

FIGURE 1. The computational set-up used to study breaking internal waves on slopes. (x_1, x_2, x_3) are Cartesian coordinates in the cross-shore, lateral (along shore, into the page) and vertical directions, respectively. (*a*) A schematic of the domain, where the length $L = 4$ m, the total depth $H = 0.56$ m, the upper-layer depth $h_1 = 0.3$ m, the lower-layer depth $h_2 = 0.26$ m, the upper-layer density $\rho_1 = 985$ kg m^{-3}, the lower-layer density $\rho_2 = 1015$ kg m^{-3}, the slope $s = 0.218$, the amplitude of the initial half-Gaussian $a_0 = 0.1$ m and the length scale of the initial half-Gaussian $L_0 = 0.7$ m. The length of the flat region before the slope begins is $L_s = 1.675$ m and the radius of curvature of the rounded bottom at the beginning of the slope is 3 m. The pycnocline thickness δ varies for each case and is shown in table 1. The lateral (x_2, into the page) width of the domain is $W = 0.1$ m. (*b*) The initial density profile for each case, as defined in (2.1). The stratified region around the interface $x_3 = -h_1 \pm \delta/4$ is highlighted by the intersection of the vertical dotted lines at $\rho/\rho_0 = 0.987$, 1.013 with each density profile. (*c*) The maximum buoyancy frequency for each case N_{max} as a function of δ, including a scaling line of $N_{max} \sim \delta^{-1/2}$ (Troy & Koseff 2005).

Research Center (ARL DSRC) supercomputer Pershing using 432 processors. With a computation time of approximately 20 s per time step, this resulted in wall-clock simulation times ranging from 100 h (43 000 processor h; case 1) to 150 h (65 000 processor h; case 8).

2.2. *Initial wave parameters*

We consider eight breaking wave cases with varying pycnocline thickness δ, as summarized in table 1. The stratification within the domain is initialized as

$$\frac{\rho}{\rho_0}(x_1, x_3, \tau = 0) = 1 - \frac{\Delta\rho}{2\rho_0} \tanh\left[\frac{2(x_3 + h_1 + \zeta(x_1))}{\delta} \tanh^{-1}(\alpha)\right], \qquad (2.1)$$

Case	δ (cm)	a (cm)	c (m s^{-1})	L_w (m)	$k\delta$	ka	Re_w
1	2	4.9	0.16	1.27	0.05	0.12	146
2	10	4.9	0.16	1.25	0.25	0.12	159
3	20	5.0	0.16	1.23	0.51	0.13	162
4	30	5.1	0.16	1.21	0.78	0.13	167
5	40	5.1	0.15	1.20	1.04	0.13	162
6	50	5.2	0.14	1.20	1.31	0.14	151
7	60	5.2	0.12	1.20	1.57	0.14	138
8	70	5.2	0.12	1.20	1.83	0.14	137

TABLE 1. The breaking wave cases considered in this study in terms of the pycnocline thickness δ, the wave amplitude a, the wave speed c and the wave length scale L_w, the normalized interface thickness $k\delta$, the wave steepness ka and the wave Reynolds number Re_w.

where the reference density $\rho_0 = 1000$ kg m^{-3}, the density difference between the top and bottom layers is $\Delta\rho = \rho_2 - \rho_1 = 30$ kg m^{-3}, the upper-layer depth $h_1 = 0.3$ m, and $\alpha = 0.99$. The pycnocline thickness δ determines the buoyancy frequency $N = \sqrt{-(g/\rho_0)\partial\rho/\partial x_3}$ of the initial stratification; the maximum buoyancy frequency N_{max} scales with $\delta^{-1/2}$ (Troy & Koseff 2005), as is shown for each case in figure 1(*c*). Throughout the paper, we refer to time using the variable τ in order to avoid confusion with t, which stands for 'turbulent' in the notation of Scotti & White (2014).

A wave of depression is created in the domain by initializing a half-Gaussian at the left boundary. The shape of the interface is given by

$$\zeta(x_1) = a_0 \exp\left[-\left(\frac{x_1}{L_0}\right)^2\right] + \zeta' R, \tag{2.2}$$

where $a_0 = 0.1$ m and $L_0 = 0.7$ m are the initial amplitude and length scale of the half-Gaussian, respectively. An initial perturbation $\zeta' R$, where $\zeta' = 1$ mm and $R \in \{-1, 1\}$ is a uniformly distributed random number, is also added to the interface to trigger lateral instabilities during breaking. Relaxation of the initial half-Gaussian produces an internal wave of depression that propagates toward the slope and breaks. We note that the initial wave is solitary-like, but that it does not necessarily satisfy the Dubreil–Jacotin–Long (DJL) equation for internal solitary waves (see Lamb 2002, and references therein). We therefore refer to the waves in this study more generally as 'internal waves'. Further discussion of the difference between the waves in the present study and true DJL internal solitary waves can be found in Arthur & Fringer (2016).

Here, case 1 corresponds to case 3 from Arthur & Fringer (2014) and cases 3t1/3t2 from Arthur & Fringer (2016). The additional cases 2–8 differ from this 'base case' only in the value of δ; all other initial parameters are held constant. As a result of changing δ, the other properties of the incoming wave (after it has formed from the initial half-Gaussian) change slightly relative to the base case (see table 1). These properties, including the wave amplitude a, the wave speed c and the wave length scale $L_w = 1/a \int_0^{L_x} \eta(x_1)\,\mathrm{d}x_1$, where η is the displacement of the $\rho = \rho_0$ isopycnal from $x_3 = -h_1$ (Michallet & Ivey 1999), are calculated after the wave has formed but before it begins to interact with the slope.

In order to quantify the effect of changing the pycnocline thickness δ on the incoming wave, we classify each breaking wave case in terms of the relevant non-dimensional parameters, including $k\delta$, ka and Re_w (Troy & Koseff 2005), as shown in table 1: $k\delta$ is the normalized pycnocline thickness, where the horizontal wavenumber $k = 2\pi/\lambda$ and $\lambda \approx 2L_w$; ka is the wave steepness; $Re_w = a^2\omega/\nu$ is the wave Reynolds number, where the wave frequency $\omega = c/\lambda$. We note that the value of $Re_w = 146$ reported here for case 1 differs from the value of $Re_w = 208$ reported for the same case in Arthur & Fringer (2014) and Arthur & Fringer (2016). Here, we use the actual wave speed c as opposed to the linear phase speed in a two-layer system that was used previously. As shown in table 1, the normalized pycnocline thickness varies by nearly two orders of magnitude from case 1 to case 8. However, ka and Re_w change by no more than 20 % from the base case. The bathymetric slope s is also held constant. We therefore focus our analysis on how the energetics of wave breaking change with the normalized pycnocline thickness $k\delta$. Troy & Koseff (2005) considered the combined effect of the pycnocline thickness $k\delta$ and the wave steepness ka using the wave Richardson number $Ri_w \sim k\delta/(ka)^2$. However, we do not consider Ri_w here because ka is roughly constant and therefore $Ri_w \sim k\delta$.

3. General description of wave breaking

The density structure over the course of the breaking event is similar for each case, and is shown in figure 2 for case 5 ($k\delta \approx 1$). In this figure and others, we present the time τ normalized by the wave period for case 1, $T_1 = 2\pi/\omega_1$. As the wave begins to interact with the slope, downslope flow is concentrated in the lower layer beneath the leading face (figure 2*a*). At the same time, the rear face steepens (figure 2*b*). The downslope flow beneath the leading face and the upslope flow beneath the rear face then interact to create the shear that initializes the breaking event (figure 2*c*).

After breaking, a surge of dense fluid flows up the slope, creating shear instabilities (billows) at the interface (figure 2*d*,*e*). These billows create regions of unstable stratification that are subject to secondary convective instability. A region of unstable stratification is also created under the nose of the upslope surge, leading to the lobe and cleft instability typical of gravity currents (Simpson 1972; Härtel, Carlsson & Thunblom 2000). Figure 3 shows the development of lateral instabilities in these two regions after breaking for case 5. A three-dimensional view of the upslope surge that depicts the fully turbulent flow field for case 5 is shown in figure 4. After the upslope surge reaches its maximum onshore position (figure 2*f*), dense fluid flows back downslope (figure 2*g–i*) and the pycnocline returns to approximately its initial horizontal position (figure 2*i*). As in Arthur & Fringer (2014, 2016), we define the end of the breaking event τ_f as the time just before dissipation begins to rise due to a second upslope surge of dense fluid (see figure 9*a*). This second upslope surge arises from small waves trailing behind the initial wave due to the initial condition, but is not considered in our results.

All of the breaking waves in this study can be classified as ‘collapsing breakers’ (Boegman *et al.* 2005; Aghsaee, Boegman & Lamb 2010; Arthur & Fringer 2014) or ‘backward overturning’ (Moore, Koseff & Hult 2016) since the steepening rear face is swept (collapses) backward before it is able to plunge forward. However, several differences can be seen in the breaking event among cases 1–8. The first occurs just before the backward collapse, as a tongue of dense water is forced into the interior of the water column by the upslope momentum of the wave. This dense tongue becomes larger as $k\delta$ increases (see figure 5*a–h*). Additionally, during the upslope

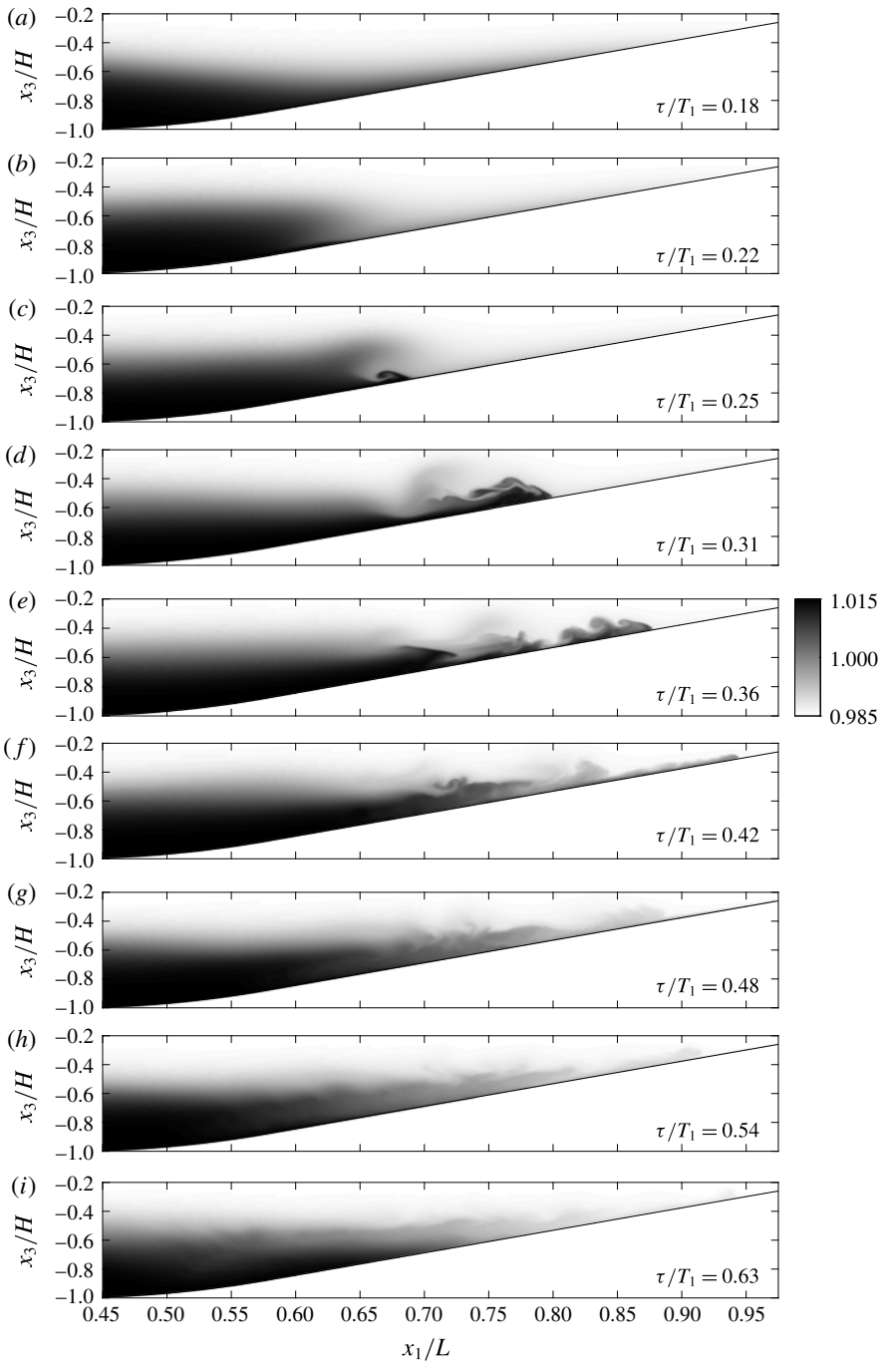

FIGURE 2. Snapshots in time of the density structure ρ/ρ_0 for breaking wave case 5 ($k\delta \approx 1$). Results are averaged in the lateral (x_2) direction. The time shown in (c) represents the breakpoint, shown in figure 5(e), while the time shown in (e) represents the time of maximum turbulent mixing $(\epsilon_p^t)^V_{max}$ (5.2), shown in figures 4 and 5(m).

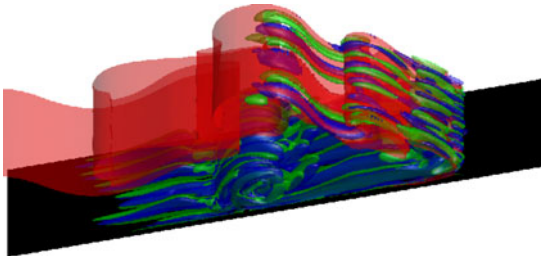

FIGURE 3. A three-dimensional view of lateral instabilities developing after breaking for case 5 ($k\delta \approx 1$), corresponding to figure 2(*d*). Isosurfaces of $\rho = \rho_0$ (red), $\Omega_1/\omega_1 = 24$ (blue) and $\Omega_1/\omega_1 = -24$ (green) are shown. Ω_1 is the longitudinal vorticity, representing the 'streamwise rolls' discussed in Arthur & Fringer (2014).

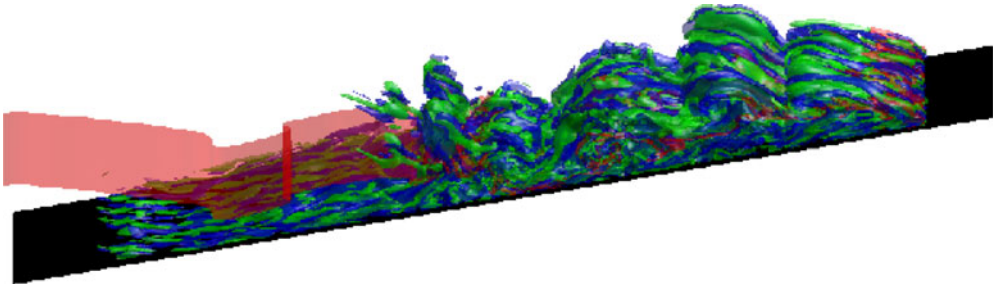

FIGURE 4. A three-dimensional view of the turbulent flow field during the upslope surge for case 5 ($k\delta \approx 1$), corresponding to figures 2(*e*) and 5(*m*). Isosurfaces of $\rho = \rho_0$ (red), $\Omega_1/\omega_1 = 37$ (blue) and $\Omega_1/\omega_1 = -37$ (green) are shown.

surge (figure 5*i–p*), the vertical length scale of the billows at the interface changes with $k\delta$. Specifically, as $k\delta$ increases, the billows appear larger relative to the height of the upslope surge. The effects of this change in scale will be discussed further in § 6.

4. Local turbulent energetics

4.1. *Local definitions of turbulent dissipation, mixing and mixing efficiency*

The local mixing efficiency of stratified turbulent flows has traditionally been quantified using the flux Richardson number $R_f = \mathcal{B}/(\mathcal{B} + \epsilon)$ (1.1), where $\mathcal{B} = (g/\rho_0)\overline{\rho' u_3'}$ is the turbulent buoyancy flux and $\epsilon = 2\nu\overline{S_{ij}' S_{ij}'}$ is the turbulent dissipation (e.g. Osborn 1980; Ivey & Imberger 1991; Shih *et al.* 2005). The turbulent rate of strain tensor is $S_{ij}' = ((\partial u_i'/\partial x_j) + (\partial u_j'/\partial x_i))/2$. The overbar denotes a Reynolds average, while the prime denotes a departure from that average. As discussed by Venayagamoorthy & Koseff (2016), the turbulent buoyancy flux $\mathcal{B}$ can include reversible countergradient fluxes, leading to low or negative values of R_f, especially in weakly turbulent conditions. Interpretation of R_f using this method is further complicated in the presence of unsteady, inhomogeneous turbulence due to the difficulty in choosing the appropriate Reynolds average (e.g. Hult *et al.* 2011). Thus, even in the current DNS study, it is difficult to interpret the meaning of R_f.

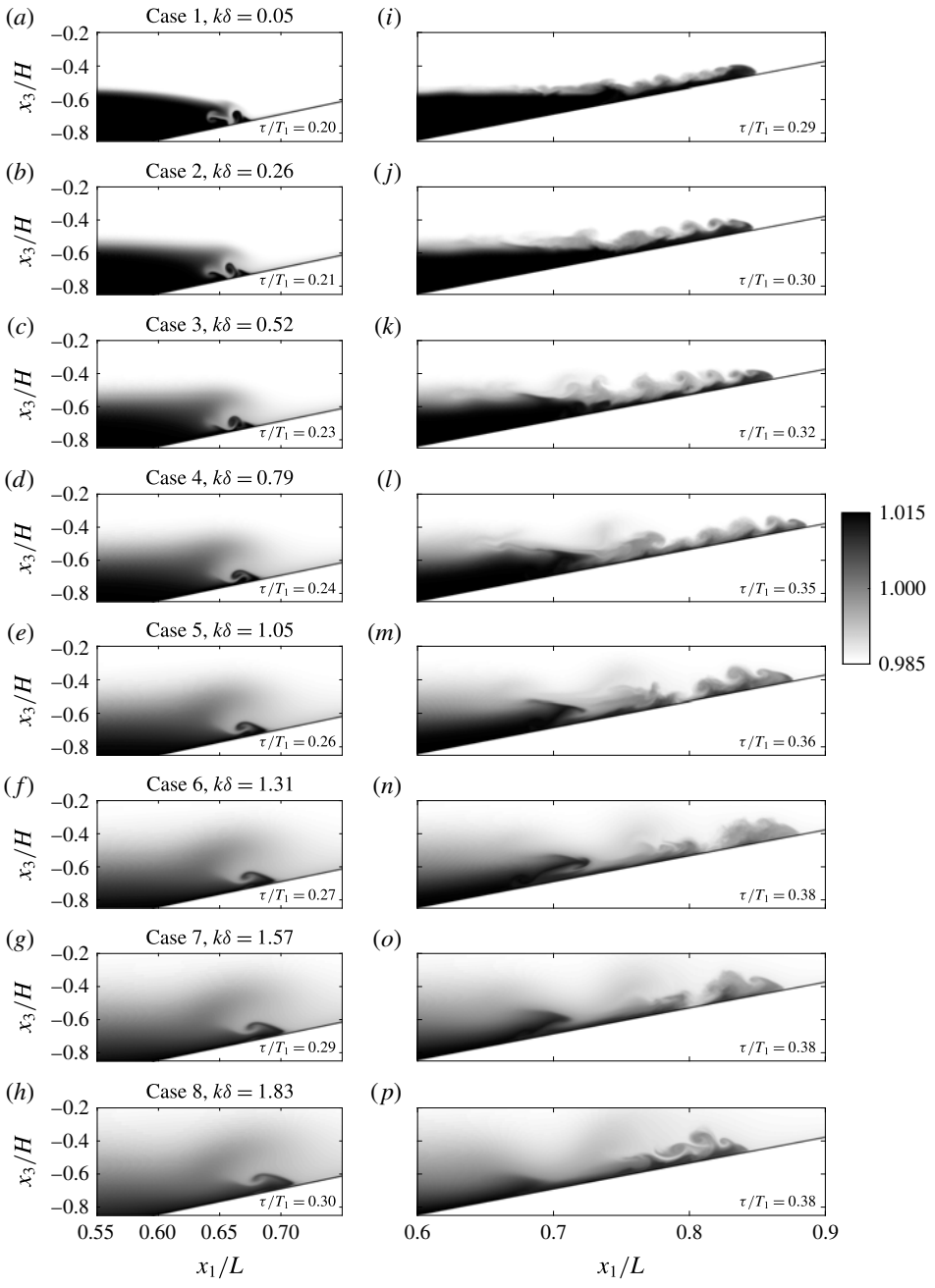

FIGURE 5. Snapshots of the density structure ρ/ρ_0 for breaking wave cases 1–8. Results are averaged in the lateral (x_2) direction. Column (*a–h*) depicts the wave at the time of breaking, while column (*i–p*) shows the upslope surge of dense fluid after breaking at the time of maximum turbulent mixing $(\epsilon_p^t)_{max}^V$ (5.2).

To address the problems associated with quantifying turbulent dissipation, mixing and mixing efficiency in regions of unsteady, inhomogeneous turbulence, Scotti & White (2014) developed a new method of analysis based on a locally defined

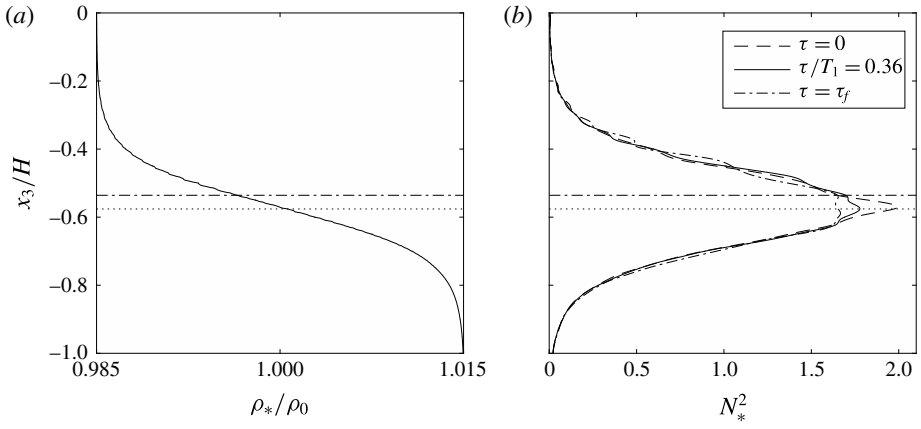

FIGURE 6. (*a*) The background density field ρ_*/ρ_0 and (*b*) the background buoyancy frequency field N_*^2 used in the calculation of ϵ_p^t. Data are shown for case 5 ($k\delta \approx 1$) at the time of maximum turbulent mixing $(\epsilon_p^t)_{max}^V$ (5.2), which corresponds to the time shown in figures 2(*e*), 4 and 5(*m*). The background buoyancy frequency is shown at $\tau = 0$ and $\tau = \tau_f$ in (*b*) as well. The horizontal dotted line denotes the vertical location of the maximum background buoyancy frequency N_*^2 at $\tau/T_1 = 0.36$, while the horizontal dash-dot line denotes the vertical location of the initial pycnocline $x_3 = -h_1$.

background potential energy. Their method builds upon the background potential energy framework of Winters *et al.* (1995) to define local turbulent dissipation and irreversible turbulent mixing quantities. Turbulent dissipation is defined as above,

$$\epsilon_k^t = 2\nu\overline{S'_{ij}S'_{ij}}, \tag{4.1}$$

where we have adopted the notation of Scotti & White (2014) for clarity. Irreversible turbulent mixing is defined as the turbulent dissipation of available potential energy,

$$\epsilon_p^t = \kappa\left(\frac{\overline{|\nabla b|^2}}{N_*^2(b)} - \frac{|\nabla\overline{b}|^2}{N_*^2(\overline{b})}\right) \simeq \kappa\frac{\overline{|\nabla b'|^2}}{N_*^2(\overline{b})}, \tag{4.2}$$

where $b(x_1, x_2, x_3, \tau) = g(\rho - \rho_0)/\rho_0$ is the buoyancy field and $N_*^2(x_3, \tau)$ is the squared buoyancy frequency of the background density field $\rho_*(x_3, \tau)$. The background density field represents the lowest possible potential energy state of the system if it were to be adiabatically rearranged (Winters *et al.* 1995), and is obtained numerically by sorting the density field ρ. Changes in the background potential energy can only occur due to molecular diffusion, and are therefore irreversible. In the present study, the Reynolds average overbar denotes a lateral average (in the x_2 direction), while the prime denotes a departure from that average. Our calculations of ϵ_k^t and ϵ_p^t are therefore functions of x_1, x_3 and τ. In (4.2), $N_*^2(b)$ is found by mapping the given local value of b to a corresponding value of N_*^2 in the background buoyancy frequency profile and is therefore a function of x_1, x_2, x_3 and τ. Alternatively, $N_*^2(\overline{b})$ must be found by interpolating N_*^2 to the given value of $\overline{b}$, and is therefore a function of x_1, x_3 and τ.

Irreversible mixing leads to a decrease in the maximum background buoyancy frequency over time. This is shown in figure 6, which presents example calculations

of the background density field ρ_* and background buoyancy frequency field N_*^2 for case 5. The background buoyancy frequency is shown for the initial condition $\tau = 0$, during the upslope surge at $\tau/T_1 = 0.36$ (the time shown in figures 2*e*, 4 and 5*m*), and at the end of the breaking event $\tau = \tau_f$. The background density field is only shown for the intermediate time $\tau/T_1 = 0.36$ because the change from $\tau = 0$ to $\tau = \tau_f$ is not discernible in the figure. The horizontal dotted line denotes the vertical location of the maximum buoyancy frequency at $\tau/T_1 = 0.36$, which is slightly below $x_3 = -h_1$ because there is initially less lower-layer fluid ($\rho = \rho_2$) than upper-layer fluid ($\rho = \rho_1$) in the domain due to the sloping bottom. Layering is also evident in the background density field (figure 6*a*), along with the corresponding wiggles in N_*^2 (figure 6*b*).

Using the definitions of turbulent dissipation and irreversible turbulent mixing in (4.1) and (4.2) above, the local irreversible flux Richardson number can be calculated with

$$R_f^* = \frac{\epsilon_p^t}{\epsilon_p^t + \epsilon_k^t}. \tag{4.3}$$

This measure of the flux Richardson number is not affected by countergradient buoyancy fluxes, and is therefore a preferable measure of the local mixing efficiency to R_f (Scotti & White 2014; Venayagamoorthy & Koseff 2016).

Local turbulent dissipation and irreversible mixing quantities are calculated over time for each breaking wave case. For illustrative purposes, we consider these quantities for case 5 during the upslope surge of dense fluid after breaking, when shear instabilities (billows) are present at the interface (figure 7*a*). At this time, turbulent dissipation ϵ_k^t and mixing ϵ_p^t are elevated throughout the upslope surge (figure 7*b*,*c*). However, mixing is more concentrated along the roll-up regions of the billows and the nose of the upslope surge (figure 7*c*), where sharp density gradients are present. A similar result was noted by Smyth *et al.* (2001), who used the dissipation rate of scalar variance $\chi = 2\kappa\overline{|\nabla\rho'|^2}$ to examine turbulent mixing during the breakdown of Kelvin–Helmholtz billows. The quantity χ is related to ϵ_p^t by the background buoyancy frequency N_*^2, *viz.*

$$\epsilon_p^t = \frac{g^2}{2\rho_0^2 N_*^2}\chi. \tag{4.4}$$

The local irreversible flux Richardson number R_f^* (figure 7*d*) generally follows ϵ_p^t. It approaches 1 in the billow roll-up regions and at the nose of the upslope surge, where ϵ_p^t is elevated, and approaches 0 within the billow cores and throughout the rest of the turbulent region, where ϵ_p^t is smaller relative to ϵ_k^t. Although R_f^* clearly varies with the local characteristics of the flow, the bulk (spatially and time-averaged) R_f^* is found to be roughly 0.3 for each case. We therefore present an analysis of R_f^* using the parameter space of Mater & Venayagamoorthy (2014) in the next section.

4.2. *Local mixing efficiency analysis*

Mater & Venayagamoorthy (2014) defined three non-dimensional parameters that quantify the effects of shear, stratification and viscosity in stratified turbulence. They include a shear strength parameter ST_L, a turbulent Froude number Fr_k and a turbulent Reynolds number Re_L, as presented in § 1. Here, we define these parameters as

$$ST_L = \frac{\overline{S}k^t}{\epsilon_k^t}, \tag{4.5}$$

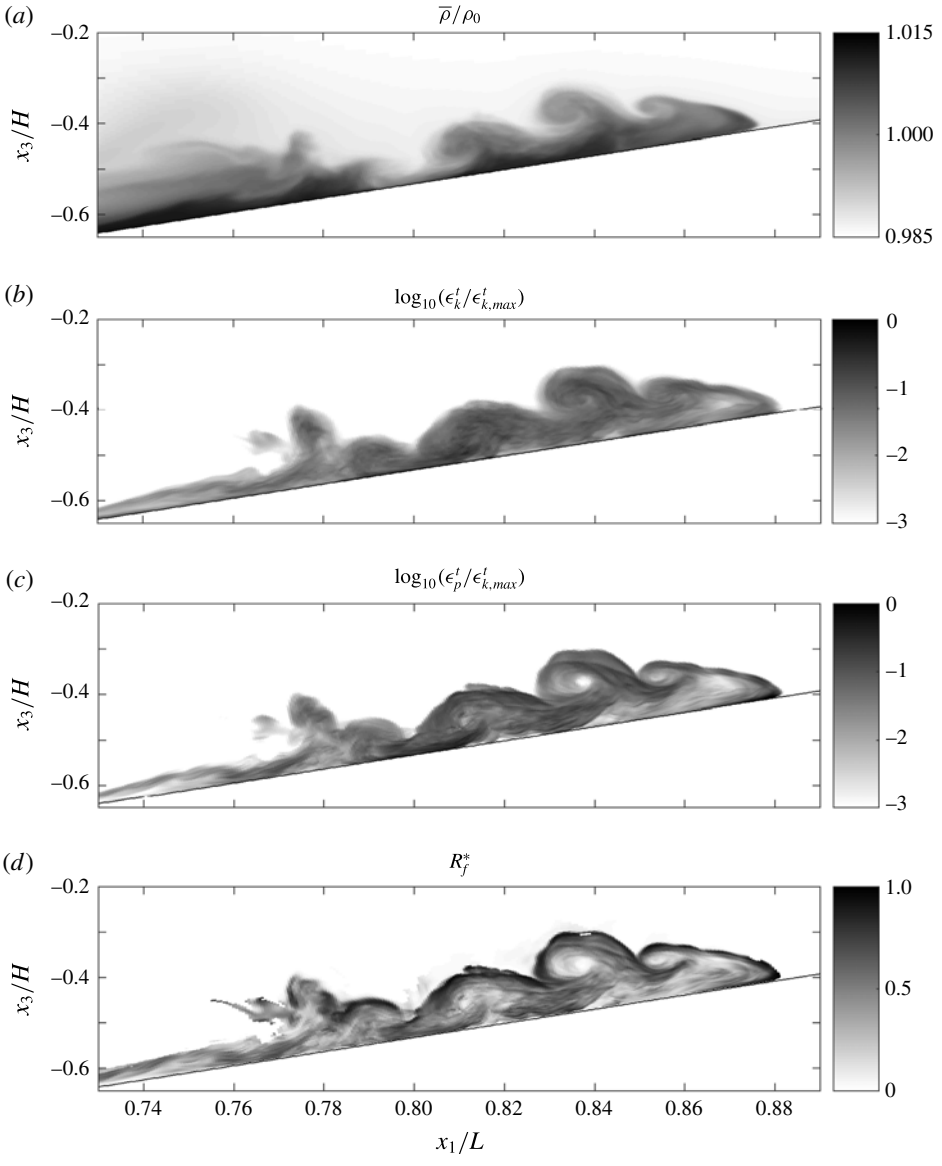

FIGURE 7. Example local turbulent energetics calculations for case 5 ($k\delta \approx 1$) at the time of maximum turbulent mixing $(\epsilon_p^t)_{max}^V$ ((5.2), corresponding to the time shown in figures 2(*e*), 4 and 5(*m*)). Shown are (*a*) the density field $\overline{\rho}/\rho_0$, (*b*) the turbulent dissipation ϵ_k^t, (*c*) the turbulent mixing ϵ_p^t, and (*d*) the local irreversible flux Richardson number R_f^*. In (*b*) and (*c*), the turbulent quantities are normalized by the maximum turbulent dissipation at the time shown, $\epsilon_{k,max}^t$. Note that in (*d*), the R_f^* field is restricted to locations where $Re_L > 10$ for clarity (Re_L is defined in (4.7)), while (*a*), (*b*) and (*c*) include the full field.

where $\overline{S} = |\partial\overline{u}_1/\partial x_3|$ is the absolute value of the laterally averaged vertical shear and $k^t = \overline{(u_i'u_i')}/2$ is the turbulent kinetic energy,

$$Fr_k = \frac{\epsilon_k^t}{N_*(\overline{b})k^t}, \tag{4.6}$$

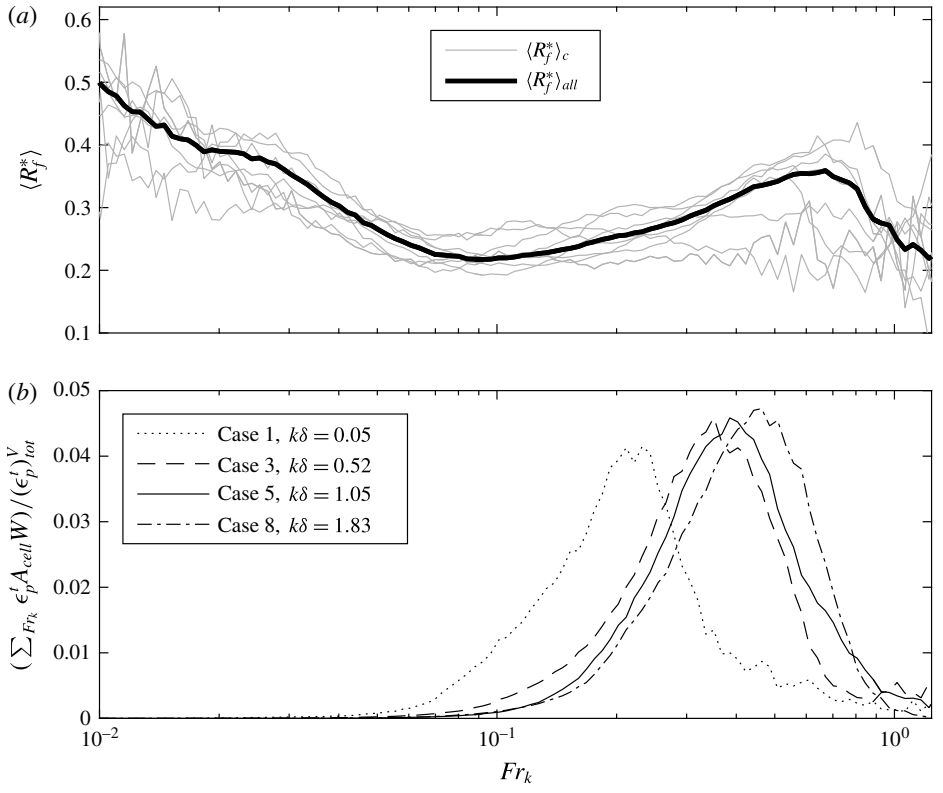

FIGURE 8. R_f^* versus Fr_k results for breaking wave cases 1–8. Data are restricted to $4 < ST_L < 9$ and $100 < Re_L < 400$. (*a*) The overall mean irreversible flux Richardson number $\langle R_f^* \rangle_{all}$ along with $\langle R_f^* \rangle_c$ for cases 1–8. (*b*) The area-weighted fraction of total turbulent mixing as a function of Fr_k (i.e. a binned sum of $\epsilon_p^t A_{cell} W/(\epsilon_p^t)_{tot}^V$ in each Fr_k bin, where A_{cell} is the (x_1, x_3) area of the corresponding grid cell and W is the x_2 width of the domain), for cases 1, 3, 5 and 8. The quantity $(\epsilon_p^t)_{tot}^V$ used in (*b*) is the total volume-integrated turbulent mixing (defined in (5.4)).

where $N_*(\bar{b})$ is the buoyancy frequency of the background density field for the local value of $\bar{b}$, as in (4.2), and

$$Re_L = \frac{(k^t)^2}{\nu \epsilon_k^t}. \tag{4.7}$$

Because we are interested in the effect of stratification on the local turbulent mixing efficiency, we consider how R_f^* varies with the turbulent Froude number Fr_k. For each breaking wave case, we calculate a mean irreversible flux Richardson number $\langle R_f^* \rangle_c$ in bins of Fr_k (figure 8*a*). $\langle R_f^* \rangle_c$ reaches a local maximum between 0.2 and 0.45 for $0.5 < Fr_k < 0.9$. We also define an overall mean irreversible flux Richardson number $\langle R_f^* \rangle_{all}$ as a function of Fr_k by calculating the mean R_f^* value among all cases in each Fr_k bin. The $\langle R_f^* \rangle_{all}$ versus Fr_k curve captures the general trends of the $\langle R_f^* \rangle_c$ versus Fr_k results (figure 8*a*). It reaches a local maximum of approximately 0.36 for $Fr_k \approx 0.7$, where the balance of turbulence and stratification leads to the optimal mixing efficiency. $\langle R_f^* \rangle_{all}$ decreases as Fr_k increases above 0.7 because there is less stratification to be mixed. As Fr_k decreases below 0.7 until roughly 0.1, $\langle R_f^* \rangle_{all}$ decreases because the increased

stratification suppresses turbulence. For $Fr_k < 0.1$, $\langle R_f^* \rangle_{all}$ increases as Fr_k decreases because ϵ_k^t approaches zero. Despite the relatively large values of $\langle R_f^* \rangle_c$ for $Fr_k < 0.1$, only a small fraction of the total mixing occurs in these regions. This is evidenced by the result in figure 8(*b*), which shows the total irreversible mixing ϵ_p^t that occurs within each Fr_k bin for cases 1, 3, 5 and 8.

We note that the data in this analysis are restricted to $4 < ST_L < 9$ and $100 < Re_L < 400$, which is where the most total mixing occurs over the course of each breaking wave event. The $\langle R_f^* \rangle_{all}$ versus Fr_k curve in figure 8(*b*) shows similarities to R_f and R_f^* versus Fr_k relationships found in previous studies (Shih 2003; Mater & Venayagamoorthy 2014), particularly for $Fr_k > 0.1$. However, a complete analysis of R_f^* in the (ST_L, Fr_k, Re_L) parameter space, which would facilitate direct comparisons to these studies, is left to future work.

5. Volume-integrated energetics

5.1. *Volume-integrated turbulent dissipation and mixing*

By volume-integrating local dissipation and mixing quantities during wave breaking, we examine the changes in turbulent energetics as a function of the initial interface thickness $k\delta$. We define the volume-integrated turbulent mixing as

$$(\epsilon_p^t)^V = \int_{V_s} \epsilon_p^t \, \mathrm{d}V, \tag{5.1}$$

where the volume of integration V_s is defined as the sloping region of the domain ($L_s \leqslant x_1 \leqslant L$, see figure 1) in order to better isolate the effects of breaking (Arthur & Fringer 2014). Maximum, cumulative and total volume-integrated turbulent mixing quantities are defined as

$$(\epsilon_p^t)^V_{max} = \max_{0 \leqslant \tau \leqslant \tau_f} \left(\left(\epsilon_p^t \right)^V \right), \tag{5.2}$$

$$(\epsilon_p^t)^V_{cum} = \int_0^\tau \left(\epsilon_p^t \right)^V \mathrm{d}\tau, \tag{5.3}$$

and

$$(\epsilon_p^t)^V_{tot} = \int_0^{\tau_f} \left(\epsilon_p^t \right)^V \mathrm{d}\tau, \tag{5.4}$$

respectively. Similar quantities are defined for turbulent dissipation by replacing ϵ_p^t with ϵ_k^t in (5.1)–(5.4). Turbulent dissipation and mixing both begin to rise after wave breaking occurs, and continue until the end of the breaking event $\tau = \tau_f$ (figure 9*a*,*b*, points d–i for case 5). Note that the volume-integrated turbulent mixing efficiency measures in figure 9(*c*,*d*) are defined and discussed in § 5.3.

The variation in volume-integrated turbulent dissipation and mixing with $k\delta$ can be summarized by examining the maximum and total values of these quantities, as shown in figures 9(*e*) and 9(*f*), respectively. Here, we define two regimes of $k\delta$ based on the peaked shape of $(\epsilon_p^t)^V_{max}$ (figure 9*e*) and the asymptotic shape of $(\epsilon_p^t)^V_{tot}$ (figure 9*f*). Regime I is defined for $k\delta < 1$, where both $(\epsilon_p^t)^V_{max}$ and $(\epsilon_p^t)^V_{tot}$ increase monotonically. Regime II is defined for $k\delta \geqslant 1$, where $(\epsilon_p^t)^V_{max}$ decreases monotonically and $(\epsilon_p^t)^V_{tot}$ asymptotes. The maximum volume-integrated turbulent dissipation $(\epsilon_k^t)^V_{max}$ does not follow the peaked shape of $(\epsilon_p^t)^V_{max}$. Rather, $(\epsilon_k^t)^V_{max}$ increases with $k\delta$ for low $k\delta$ values in regime I, and is relatively scattered as $k\delta$ increases into regime II. The total volume-integrated turbulent dissipation $(\epsilon_k^t)^V_{tot}$, however, increases monotonically with $k\delta$ through both regimes I and II.

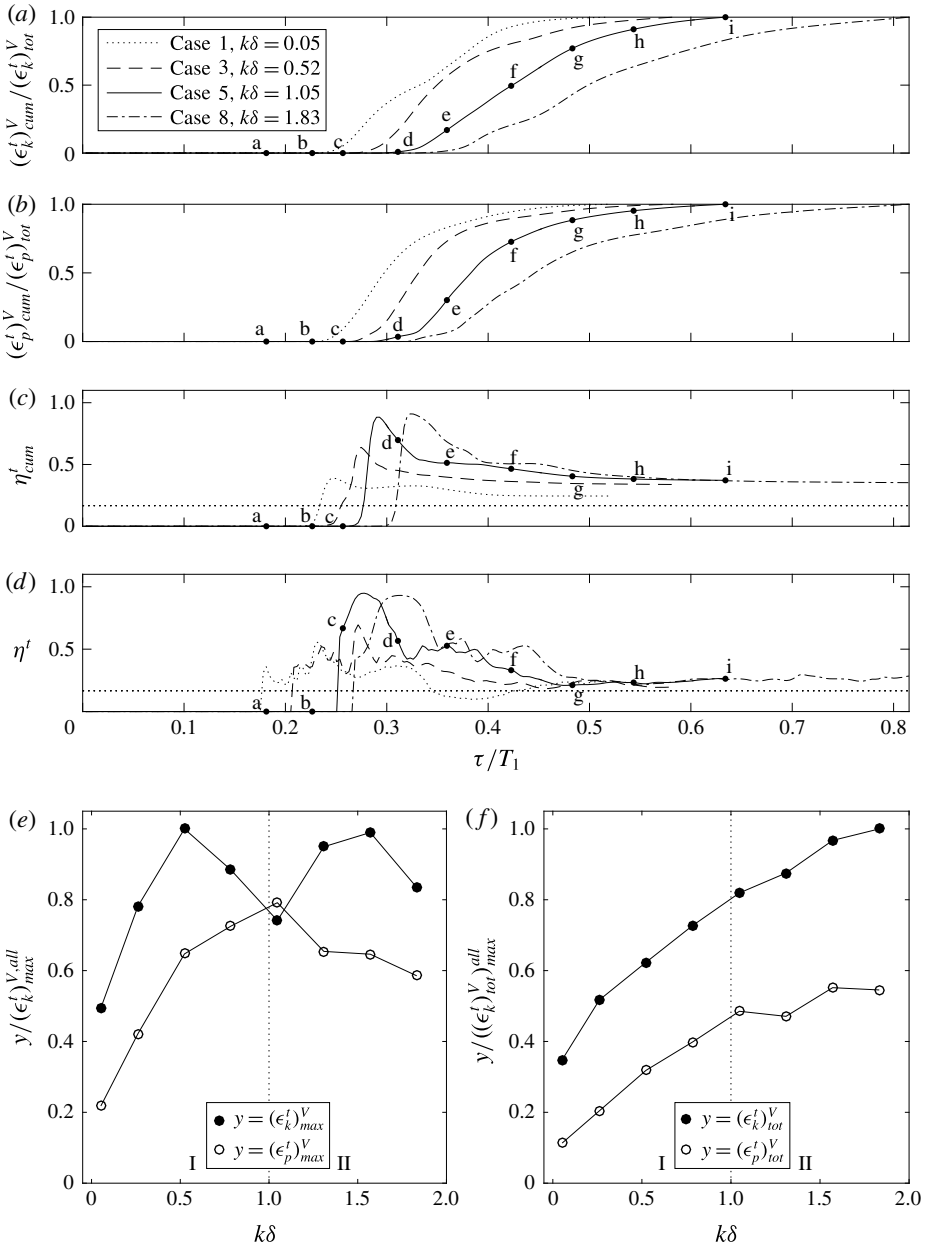

FIGURE 9. Volume-integrated turbulent energetics results for breaking wave cases 1–8. Shown are (*a*) cumulative dissipation $(\epsilon_k^t)^V_{cum}$, (*b*) cumulative mixing $(\epsilon_p^t)^V_{cum}$, (*c*) cumulative mixing efficiency η^t_{cum} and (*d*) instantaneous mixing efficiency η^t over time for cases 1, 3, 5 and 8. In (*a*) and (*b*), $(\epsilon_k^t)^V_{cum}$ and $(\epsilon_p^t)^V_{cum}$ are normalized by the total time-integrated values $(\epsilon_k^t)^V_{tot}$ and $(\epsilon_p^t)^V_{tot}$, respectively. The critical R_f value of 0.17 is shown by a horizontal dotted line in (*c*) and (*d*). Labels a–i in (*a–d*) correspond to the times shown in figure 2 for case 5. Also shown are (*e*) maximum and (*f*) total (time-integrated) values of dissipation and mixing as a function of $k\delta$ for all cases. Values in (*e*) are normalized by the maximum instantaneous turbulent dissipation for all cases $(\epsilon_k^t)^{V,all}_{max}$, while values in (*f*) are normalized by the maximum total turbulent dissipation for all cases $((\epsilon_k^t)^V_{tot})^{all}_{max}$. Vertical dotted lines in (*e*) and (*f*) represent $k\delta$ regimes I and II.

5.2. *Turbulent contribution to dissipation and mixing*

Due to the computational restrictions associated with DNS, the Reynolds number Re_w of our simulations is limited. In order to contextualize our results, it is therefore important to quantify the turbulent contribution to the full energy budget, which includes both laminar and turbulent effects. In this section, we use volume-integrated dissipation and mixing quantities to consider the turbulent contribution to the full dissipation and mixing that occurs during wave breaking. Scotti & White (2014) define the local dissipation of the full kinetic energy as

$$\epsilon_k = 2\nu S_{ij} S_{ji}, \tag{5.5}$$

where $S_{ij} = ((\partial u_i/\partial x_j) + (\partial u_j/\partial x_i))/2$ is the rate of strain tensor, see (1.1) therein. Thus, we define the full volume-integrated dissipation as

$$\mathcal{D} = \int_{V_s} \epsilon_k \, \mathrm{d}V, \tag{5.6}$$

where the volume of integration V_s is defined as in § 5.1. We define the full volume-integrated mixing as in Winters *et al.* (1995),

$$\mathcal{M} = \frac{\kappa g}{\rho_0} \left(\int_{V_s} x_3^* \frac{\partial^2}{\partial x_j \partial x_j} \rho(x_3^*) \, \mathrm{d}V - \int_A (\rho_{top} - \rho_{bottom}) \, \mathrm{d}A \right) = \phi_d - \phi_i, \tag{5.7}$$

where ϕ_d is the volume-integrated rate of change in the background potential energy and ϕ_i is the irreversible rate of change from internal to potential energy. Here, ρ_{top} and ρ_{bottom} are the densities on the top and bottom boundaries of the domain, respectively, and A is the corresponding surface area of the boundary. We note that the full volume-integrated dissipation $\mathcal{D}$ and mixing $\mathcal{M}$ measures defined here are equal to those used previously by Arthur & Fringer (2014). The dissipation ϵ in Arthur & Fringer (2014) is equal to $\mathcal{D}$ and the effective irreversible mixing ϕ_e in Arthur & Fringer (2014) is equal to $\mathcal{M}$. The values $\mathcal{D}$ and $\mathcal{M}$ include both laminar and turbulent effects, while $(\epsilon_k^t)^V$ and $(\epsilon_p^t)^V$ (5.1) include only turbulent effects.

The initial peak in the full dissipation $\mathcal{D}$ (shown for case 5 in figure 10*a*) is associated with near-bottom downslope flow in the lower layer prior to breaking (figure 2*a*). As noted in Arthur & Fringer (2014), this dissipation is laminar because turbulence does not develop in the domain until wave breaking occurs. The turbulent dissipation $(\epsilon_k^t)^V$, therefore, does not begin to rise until breaking and does not include this pre-breaking laminar dissipation. The shapes of the turbulent mixing $(\epsilon_p^t)^V$ and full mixing $\mathcal{M}$ curves (shown for case 5 in figure 10*b*) are similar. This is expected because the turbulence generated by overturning during the breaking event is the primary driver of mixing in the domain. Overall, however, $(\epsilon_k^t)^V$ and $(\epsilon_p^t)^V$ are generally lower than $\mathcal{D}$ and $\mathcal{M}$, respectively, throughout the breaking event.

In order to quantify the difference between the turbulent and full measures of dissipation and mixing, we define f_{turb} as the fraction of either dissipation or mixing due to turbulence over the course of the breaking event. Thus $f_{turb} = (\epsilon_k^t)^V_{tot}/\mathcal{D}_{tot}$ for dissipation and $f_{turb} = (\epsilon_p^t)^V_{tot}/\mathcal{M}_{tot}$ for mixing, where $\mathcal{D}_{tot}$ and $\mathcal{M}_{tot}$ are the time-integrated values of $\mathcal{D}$ and $\mathcal{M}$, respectively, defined as in (5.4) for $(\epsilon_p^t)^V_{tot}$. The turbulent contribution to dissipation (figure 10*c*) increases within regime I from approximately 17 % for case 1 to approximately 35 % for case 5 ($k\delta \approx 1$). Within regime II, f_{turb} remains relatively constant. The turbulent contribution to mixing

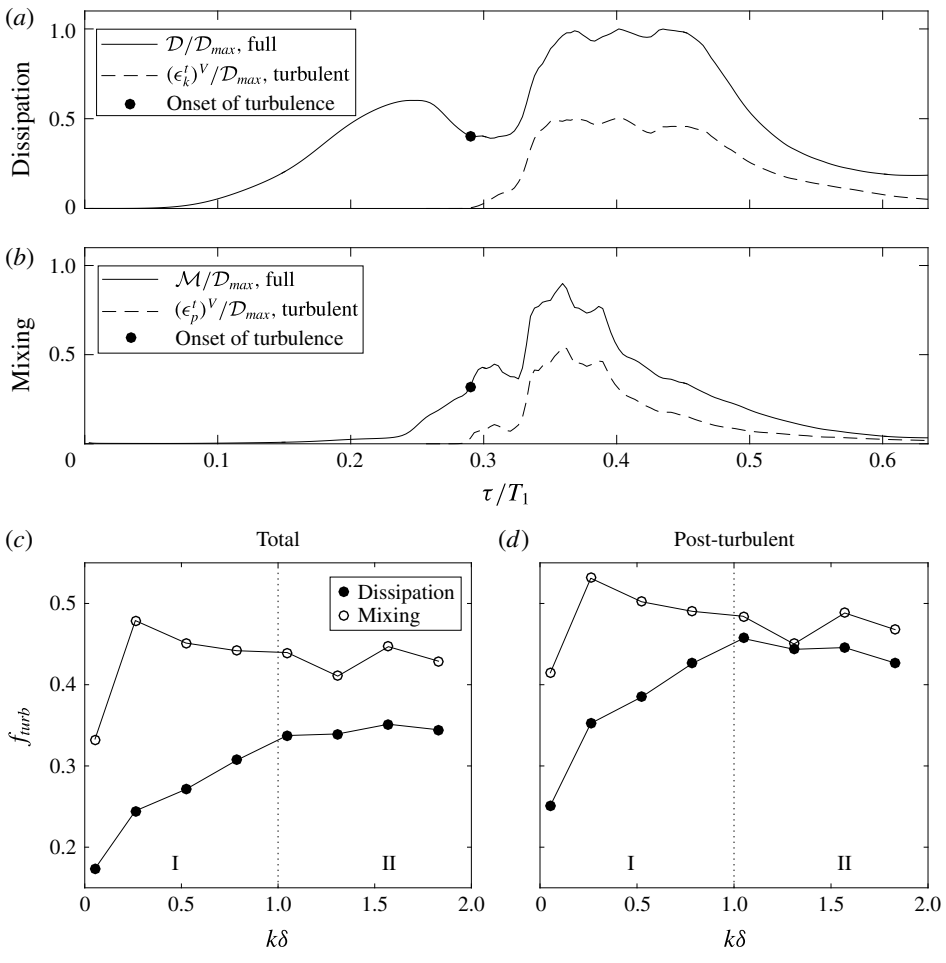

FIGURE 10. The turbulent contribution to dissipation and mixing. Volume-integrated (*a*) dissipation ($(\epsilon_k^t)^V$, turbulent and $\mathcal{D}$, full) and (*b*) mixing ($(\epsilon_p^t)^V$, turbulent and $\mathcal{M}$, full) over time for breaking wave case 5 ($k\delta \approx 1$). Values in (*a*) and (*b*) are normalized by $\mathcal{D}_{max}$, the maximum full dissipation for case 5. The fraction f_{turb} of both dissipation and mixing (*c*) over the entire breaking wave event ('Total') and (*d*) during the turbulent portion of the event ('Post-turbulent'), as a function of $k\delta$ for all cases. The vertical dotted lines in (*c*) and (*d*) represent $k\delta$ regimes I and II defined in § 5.1.

(figure 10*c*) is approximately 34 % for case 1, but is then roughly constant between 40 %–50 % for larger $k\delta$. The onset of turbulence in the domain (when $(\epsilon_k^t)^V$ and $(\epsilon_p^t)^V$ begin to rise) is indicated by a dot in figure 10(*a*,*b*). Another calculation of f_{turb}, this time over only the post-turbulent portion of the event (as opposed to the entire event) is shown in figure 10(*d*). The turbulent contributions to dissipation and mixing are higher in the post-turbulent stage because the laminar pre-breaking stage is not included, reaching approximately 45 % for dissipation and 45 %–55 % for mixing. However, similar trends are seen with $k\delta$.

Overall, the turbulent contribution to dissipation and mixing is relatively low (<60 %). This is a consequence of the low Reynolds number Re_w used in our simulations, which is necessitated by the computational restrictions associated

with DNS. Although we reach local Re_b values of the order of 10^2–10^3 (in the energetic regime of Shih *et al.* 2005), these regions make up only a small fraction of the domain. Arthur & Fringer (2014) found that as Re_w increases, the turbulent contribution to dissipation and mixing during breaking internal wave events increases because turbulence develops earlier in the event. Thus, we expect that as the Reynolds number of the cases considered in this study increases, the turbulent contribution to dissipation and mixing will also increase. The potential effect of increasing the Reynolds number on the mixing efficiency is discussed in the next section. However, further analysis at larger Reynolds number is left to future work.

5.3. *Volume-integrated mixing efficiency*

Using the volume-integrated calculations of turbulent dissipation and mixing above, volume-integrated measures of the turbulent mixing efficiency are made. We define a cumulative volume-integrated turbulent mixing efficiency

$$\eta^t_{cum}(\tau) = \frac{\displaystyle\int_0^\tau (\epsilon_p^t)^V \,\mathrm{d}\tau}{\displaystyle\int_0^\tau \left((\epsilon_p^t)^V + (\epsilon_k^t)^V\right) \mathrm{d}\tau}, \tag{5.8}$$

as well as a bulk volume-integrated turbulent mixing efficiency

$$\eta^t_B = \frac{(\epsilon_p^t)^V_{tot}}{(\epsilon_p^t)^V_{tot} + (\epsilon_k^t)^V_{tot}}. \tag{5.9}$$

Thus, $\eta^t_{cum}(\tau_f) = \eta^t_B$. As in Arthur & Fringer (2014), we also define a full bulk mixing efficiency, which includes both laminar and turbulent effects, as

$$\eta_B = \frac{\mathcal{M}_{tot}}{\mathcal{M}_{tot} + \mathcal{D}_{tot}}. \tag{5.10}$$

The cumulative mixing efficiency η^t_{cum} (figure 9*c*) is initially large due to the offset between the growth of mixing and dissipation in the early stages of turbulence. That is, as sharp density surfaces are created by turbulent strain, mixing begins to increase before turbulent dissipation occurs. This effect is discussed in Smyth *et al.* (2001), who observed a similar phenomenon in stratified shear flow turbulence. After turbulence has developed, η^t_{cum} decreases, approaching η^t_B. The bulk volume-integrated turbulent mixing efficiency η^t_B varies in the $k\delta$ regimes defined in § 5.1 (figure 11). η^t_B is low (roughly 0.25) for small $k\delta$ (case 1). As $k\delta$ increases within regime I, the mixing efficiency increases, reaching a peak of 0.37 when $k\delta \approx 1$ (case 5). Within regime II, η^t_B levels out around 0.35.

The volume-integrated bulk mixing efficiency values calculated for breaking wave cases 1–8 are consistently higher than the critical value of the flux Richardson number, $R_f^{crit} \approx 0.17$. However, we note that the instantaneous volume-integrated turbulent mixing efficiency, defined as

$$\eta^t(\tau) = \frac{(\epsilon_p^t)^V}{(\epsilon_p^t)^V + (\epsilon_k^t)^V}, \tag{5.11}$$

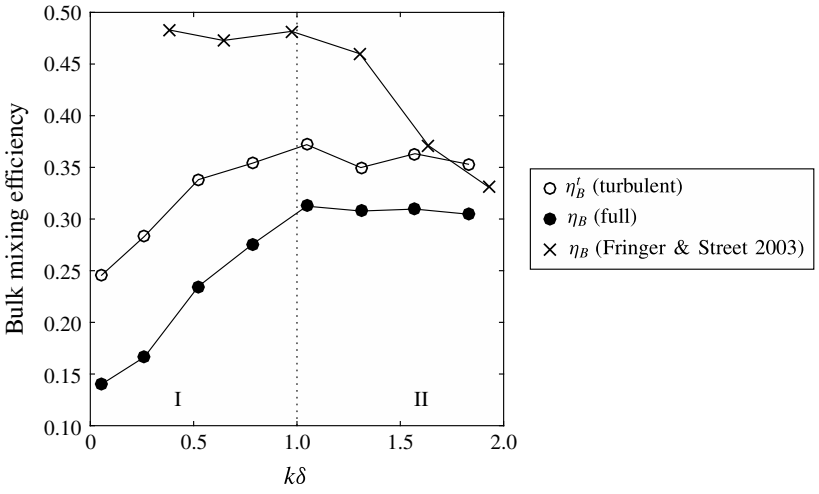

FIGURE 11. Bulk mixing efficiency measures η_B^t and η_B as functions of $k\delta$. The vertical dotted line represents $k\delta$ regimes I and II defined in § 5.1. Also shown are the bulk mixing efficiency results of Fringer & Street (2003).

and shown in figure 9(*d*), does approach $R_f^{crit} \approx 0.17$ towards the end of the breaking event, especially for low values of $k\delta$. This asymptotic behaviour occurs for each case, indicating that the turbulence after breaking reaches an equilibrium state representative of what one might expect in turbulence that is predominantly shear driven. A similar trend was observed by Smyth *et al.* (2001) for the flux coefficient, which is analogous to the mixing efficiency.

For further comparison to the present results, table 2 shows mixing efficiency values that have been calculated for various flows in previous studies. It is similar to table 1 in Fringer & Street (2003), but with the addition of several more recent studies. The range of bulk turbulent mixing efficiency values calculated here ($\eta_B^t = 0.25 - 0.37$) is on the upper end of the values reported in other studies of breaking internal waves on slopes (Michallet & Ivey 1999; Arthur & Fringer 2014). This may be because we consider only the turbulent contribution to the bulk mixing efficiency, as discussed in § 5.2. For the relatively low Reynolds number in our simulations, laminar dissipation occurs due to strong downslope flow near the bottom boundary prior to wave breaking. This laminar dissipation reduces the overall mixing efficiency of the breaking event η_B (see figure 11), but is not captured in η_B^t, which includes only turbulent effects. At higher Reynolds number, we would expect turbulence to develop earlier in the simulation (i.e. during the downslope flow of lower-layer fluid before breaking), increasing turbulent dissipation and thus lowering the turbulent mixing efficiency. Therefore, at increased Reynolds number, we would expect η_B^t and η_B to approach one another because the turbulent contribution to dissipation and mixing would overwhelm the laminar contribution.

The bulk mixing efficiency values calculated here are also larger than those presented by Hult *et al.* (2011) for breaking internal waves over a ridge. This is due, in part, to the presence of turbulence in the unstratified bottom boundary layer of their domain. Conversely, in the present breaking wave cases, the stratified region intersects the bottom boundary layer on the slope, allowing for near-bottom mixing. Because the method of Scotti & White (2014) defines turbulent dissipation and mixing locally,

Mechanism	Reference	Mixing efficiency
Rayleigh–Taylor instability	Linden & Redondo (1991)	0.5
Breaking periodic internal waves	Fringer & Street (2003)	0.42 ± 0.07
Critical topography	Slinn & Riley (1998)	$0.32 - 0.38$
Standing waves	McEwan (1983*a*)	0.26 ± 0.06
Breaking internal waves on slopes	Present	$0.25 - 0.37$
Breaking internal waves on slopes	Michallet & Ivey (1999)	$0.05 - 0.25$
Breaking internal waves on slopes	Arthur & Fringer (2014)	$0.14 - 0.20$
First principles	McEwan (1983*b*)	0.25
Critical layer	Dörnbrack (1998)	0.20
Critical layer	Lin *et al.* (1993)	0.13
Breaking interfacial waves over a ridge	Hult *et al.* (2011)	$0.04 - 0.07$
Grid turbulence	Rehmann & Koseff (2004)	0.05

TABLE 2. Mixing efficiency values from previous studies.

ϵ_k^t and ϵ_p^t can be integrated over the bottom boundary and interior regions separately. We define the bottom boundary layer as in § 2.1 as $x_3 < -d + \delta_S$, where d is the local depth, and the interior as the remainder of the domain. Although we find that 80 %–90 % of the total dissipation and mixing occur in the interior region, the bulk turbulent mixing efficiencies in both layers are similar to the overall value η_B^t (see Arthur 2015).

The present bulk mixing efficiency values are lower than those calculated by Fringer & Street (2003) for breaking progressive internal waves in deep water because of the absence of bottom boundary-layer dissipation in their domain. Fringer & Street (2003) also found a different shape of the bulk mixing efficiency as a function of $k\delta$ (see figure 11). In their study, ka is relatively large; this allows $k\delta$ to control the mixing efficiency because billows are not restricted in size by ka. Thus, weak convective breaking occurs for large $k\delta$, causing the mixing efficiency to decrease. In our simulations, ka is relatively small. Thus, the mixing efficiency is controlled by ka for large $k\delta$ (regime II), and is relatively constant. For further discussion of the billow scale in our breaking wave cases, see § 6 below.

An important consideration when comparing the present mixing efficiency calculations to those of other flows, especially in the laboratory or the field, is the Prandtl number $Pr = \nu/\kappa$. In water, $Pr = 7$ for temperature and $Pr = 700$ for salt. As Pr increases (κ decreases), one would expect the mixing efficiency to decrease because the time scale necessary for mixing to occur increases. However, $Pr = 1$ in the current simulations due to the computational restrictions associated with resolving mixing for smaller values of κ. This provides another potential explanation for the relatively high mixing efficiencies in the present study.

5.4. *Numerical effects*

Numerical effects also play a role in the energetics, and are a function of the chosen numerical methods and discretization. There are, in fact, three sources of dissipation in our simulations: that due to mean (or laminar) strains, that due to turbulent strains and that due to numerical effects. We estimate the relative magnitude of the numerical dissipation, in a domain- and time-integrated sense, by comparing the change in total energy over the course of each simulation to that captured by resolved quantities.

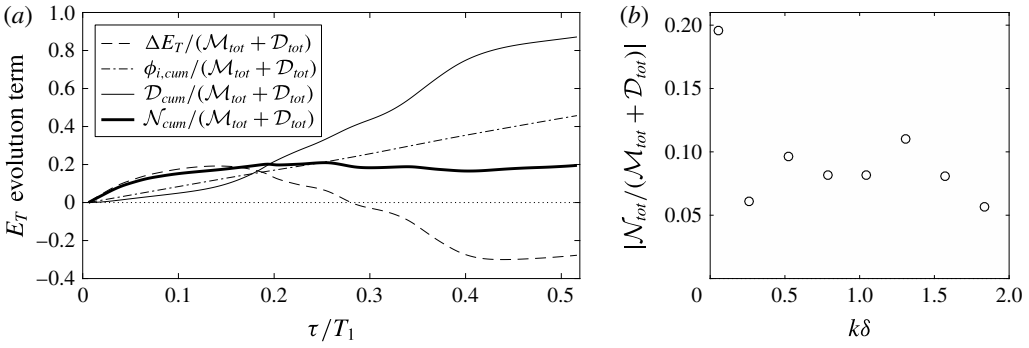

FIGURE 12. (*a*) Cumulatively integrated E_T evolution terms from (5.14) over time for case 1, normalized by $(\mathcal{M}_{tot}+\mathcal{D}_{tot})$. (*b*) Domain- and time-integrated estimate of numerical dissipation $\mathcal{N}_{tot}$ relative to the resolved full dissipation and mixing $(\mathcal{M}_{tot}+\mathcal{D}_{tot})$, as a function of $k\delta$.

Following Winters *et al.* (1995) and Arthur & Fringer (2014), the total energy is defined as

$$E_T = \frac{1}{2}\int_{V_d} u_i u_i \,\mathrm{d}V + \frac{g}{\rho_0}\int_{V_d} \rho x_3 \,\mathrm{d}V = E_K + E_P, \tag{5.12}$$

where V_d is the full volume of the domain, E_K is the kinetic energy and E_P is the potential energy. The evolution of E_T should satisfy

$$\frac{\mathrm{d}E_T}{\mathrm{d}\tau} = \phi_i - \mathcal{D} \tag{5.13}$$

because there are no boundary fluxes (Winters *et al.* 1995). Numerical dissipation can therefore be estimated as the difference between the total energy change and the resolved energy change,

$$\mathcal{N}_{cum} = \int_0^\tau \left(\frac{\mathrm{d}E_T}{\mathrm{d}\tau} - \phi_i + \mathcal{D}\right)\mathrm{d}\tau = \Delta E_T - \phi_{i,cum} + \mathcal{D}_{cum}. \tag{5.14}$$

As shown in figure 12(*a*) for case 1, the majority of the numerical dissipation occurs prior to wave breaking ($\tau/T_1 < 0.2$), as the initial wave evolves on the coarse, offshore portion of the grid.

The total domain- and time-integrated numerical dissipation can be estimated as $\mathcal{N}_{tot} = \mathcal{N}_{cum}(\tau_f)$, allowing us to estimate the effect of numerical dissipation on the full bulk mixing efficiency η_B (5.10). We define an effective full bulk mixing efficiency as

$$\eta_{B,eff} = \frac{\mathcal{M}_{tot}}{\mathcal{M}_{tot}+\mathcal{D}_{tot}+\mathcal{N}_{tot}}, \tag{5.15}$$

$$= \frac{\mathcal{M}_{tot}}{\mathcal{M}_{tot}+\mathcal{D}_{tot}\left(1+\dfrac{\mathcal{N}_{tot}}{\mathcal{M}_{tot}+\mathcal{D}_{tot}}\right)}, \tag{5.16}$$

$$= \frac{\eta_B}{1+\dfrac{\mathcal{N}_{tot}}{\mathcal{M}_{tot}+\mathcal{D}_{tot}}}. \tag{5.17}$$

Because $1/(1-r) = 1 + r + r^2/2 + \cdots$, equation (5.17) can be simplified to

$$\eta_{B,eff} \approx \eta_B \left(1 - \frac{\mathcal{N}_{tot}}{\mathcal{M}_{tot} + \mathcal{D}_{tot}}\right). \tag{5.18}$$

For cases 2–8, the quantity $|\mathcal{N}_{tot}/(\mathcal{M}_{tot} + \mathcal{D}_{tot})|$ varies between 0.06–0.11 (figure 12*b*), indicating that $\eta_{B,eff}$ is within approximately 6 %–11 % of η_B. For case 1, which has the smallest value of $k\delta$, the value of $\mathcal{N}_{tot}/(\mathcal{M}_{tot} + \mathcal{D}_{tot})$ is slightly larger in magnitude (approximately 0.2). However, as noted above in reference to figure 12(*a*), the majority of the numerical dissipation occurs prior to wave breaking. Although case 1 is shown in figure 12(*a*) because it has the largest amount of numerical dissipation, cases 2–8 show qualitatively similar results as a function of time. The overall findings of this paper related to the bulk mixing efficiency would not change despite the relatively large effect of numerical dissipation in case 1. In particular, the numerical dissipation would act to further decrease the bulk mixing efficiency for case 1, which already possesses the smallest bulk mixing efficiency among all cases.

The numerical dissipation in our simulations is due to the non-conservative energy behaviour of non-staggered grid methods, which do not allow the discrete form of the energy flux related to pu_i (where p is the pressure) to be written in conservative form (Ferziger & Perić 2002). It is therefore related to the projection scheme used by Zang *et al.* (1994) and not to numerical diffusion of momentum, which is expected because momentum advection is computed with the dispersive QUICK scheme (Leonard 1979). Based on numerical tests (not shown), ϕ_i and $\mathcal{D}$ are relatively weak functions of the grid spacing and time step size, while $\mathcal{N}$ is a relatively strong function of these parameters. This suggests that if we had the computational resources to perform the simulations with higher resolution and a smaller time step size, the effective bulk mixing efficiency $\eta_{B,eff}$ would converge to the reported bulk mixing efficiency η_B. Such higher-resolution simulations would also allow for a grid-resolution study of the dissipation spectra, a more rigorous method for assessing numerical dissipation.

6. Connecting local and volume-integrated energetics

Thus far, we have calculated both local and volume-integrated measures of turbulent energetics and mixing efficiency during breaking internal wave events on slopes. The local turbulent mixing efficiency (in terms of $\langle R_f^* \rangle_c$) varies with the local turbulent Froude number Fr_k. However, there is no clear dependence of the $\langle R_f^* \rangle_c$ versus Fr_k curves on the initial interface thickness $k\delta$, as they all generally follow $\langle R_f^* \rangle_{all}$ (figure 8*a*). Alternatively, the bulk turbulent mixing efficiency η_B^t does depend on $k\delta$ (figure 11).

Ultimately, we seek to explain the dependence of η_B^t on $k\delta$ by understanding how $k\delta$ affects the local turbulence that drives mixing. We hypothesize that because η_B^t depends on the total mixing that occurs over the course of a breaking event, it should be related to the turbulent Froude number Fr_k at which the maximum fraction of the total mixing occurs. We therefore define Fr_k^{max} as the value of Fr_k corresponding to the peak of the $(\sum_{Fr_k} \epsilon_p^t A_{cell} W)/(\epsilon_p^t)_{tot}^V$ versus Fr_k curves shown in figure 8(*b*). As presented in figure 13(*a*), Fr_k^{max} is indeed related to $k\delta$; Fr_k^{max} generally increases with $k\delta$ as the background stratification decreases. Furthermore, Fr_k^{max} can be used to predict the bulk turbulent mixing efficiency η_B^t for cases 1–8 (figure 13*b*). η_B^t is maximized when $Fr_k^{max} \approx 0.4$.

Physically, the control that $k\delta$ places on Fr_k^{max} can be described in terms of the vertical length scale of the billows that form at the density interface during wave

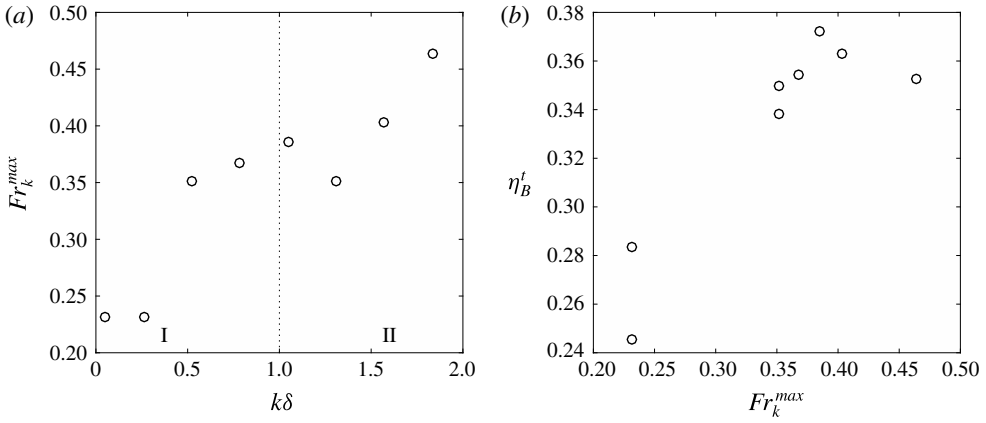

FIGURE 13. (*a*) The Fr_k of maximum mixing Fr_k^{max} as a function of $k\delta$ and (*b*) the bulk turbulent mixing efficiency η_B^t as a function of Fr_k^{max}. The vertical dotted line in (*a*) represents $k\delta$ regimes I and II defined in § 5.1.

breaking. We define $L_b(x_1)$ as the vertical length scale of the region defined by $Re_L > 100$ at the time of maximum volume-integrated turbulent mixing $(\epsilon_p^t)_{max}^V$. This region is shown in figure 14(*a–c*) for cases 1, 5 and 8, respectively. For each case, the height of the upslope surge above the bottom boundary at this time is approximately equal to a, the incoming wave amplitude (indicated by the dashed line in figure 14*a–c*). We therefore normalize L_b^{max} by $2a$ in figure 14(*d*,*e*) in order to determine when the billow scale is affected by the bottom.

For small $k\delta$, L_b is controlled by the thickness of the interface because billows are confined to the thin stratified region (figure 14*a*). Thus, $L_b^{max}/2a < 1$ (figure 14*d*, regime I), and Fr_k^{max} is relatively small (figure 14*e*). As $k\delta$ increases and the interface thickens, $L_b^{max}/2a$ and thus Fr_k^{max} increase as well. For case 5 ($k\delta \approx 1$), $L_b^{max}/2a \approx 1$ and $Fr_k^{max} \approx 0.4$, indicating the optimal transfer of energy from the large-scale wave into the billows that generate turbulence (figure 14*b*), and thus the maximum bulk mixing efficiency. As $k\delta$ increases above 1, the billows continue to grow in scale (figure 14*c*). The vertical scale $L_b^{max}/2a$ increases above 1 (figure 14*d*, regime II) and Fr_k^{max} increases above the optimal value of approximately 0.4. In regime II, The billows are clearly affected by the bottom, as $L_b^{max}/2a > 1$. This restriction on the billow scale likely leads to the asymptotic trend in the bulk mixing efficiency measures η_B^t and η_B seen in figure 11. As $k\delta$ increases above the values considered in this study, we would expect $L_b^{max}/2a$ to asymptote and Fr_k^{max} to increase, leading to a decrease in the bulk mixing efficiency. However, we note that the increase in $k\delta$ was limited in order to keep the other relevant non-dimensional parameters (ka and Re_w) relatively fixed (see § 2.2).

7. Conclusions

Using DNS, we have explored local and volume-integrated measures of turbulence and mixing in breaking internal waves on slopes. We considered eight breaking wave cases with a range of normalized pycnocline thicknesses $k\delta$, but with similar incoming wave properties (ka, Re_w). Thus, for a similar incoming wave and constant bathymetric slope, we examined the effect of stratification on energetics and mixing efficiency. This effect is relevant in lakes and the coastal ocean, where the stratification

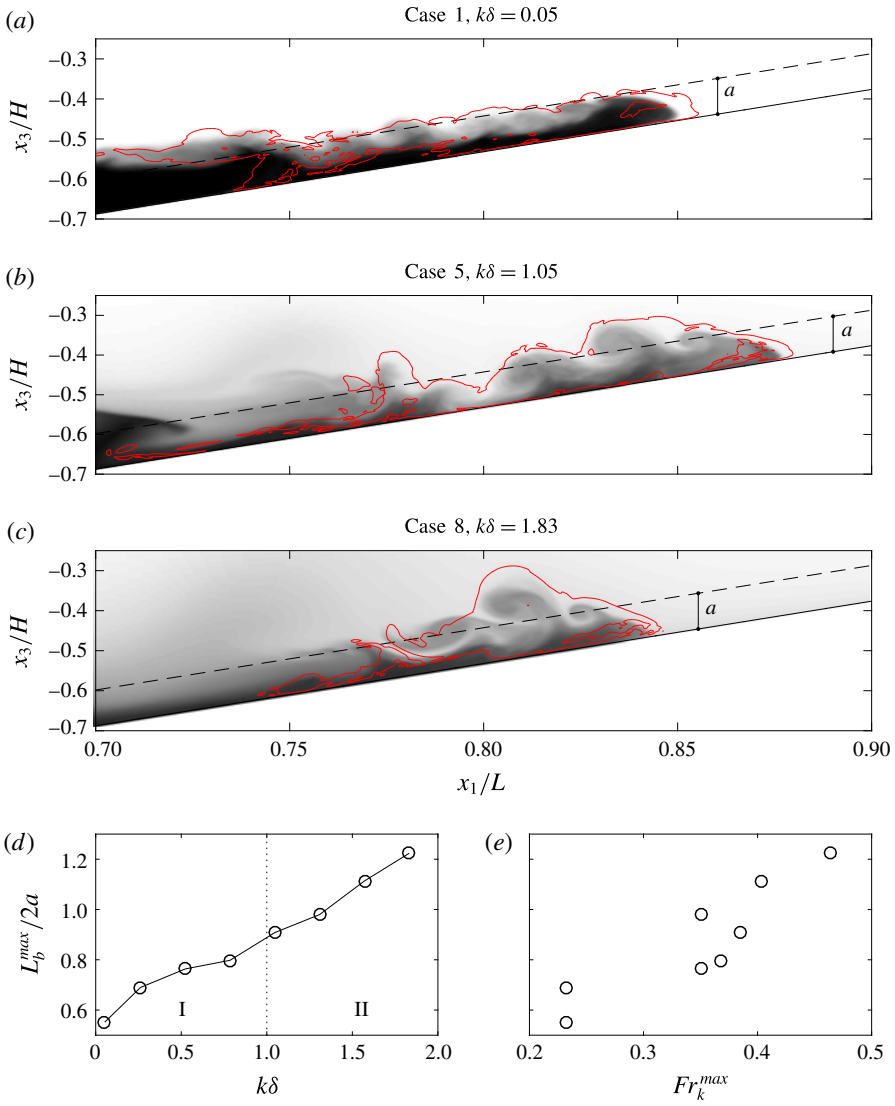

FIGURE 14. The vertical length scale L_b of the billows at the interface at the time of maximum volume-integrated turbulent mixing $(\epsilon_p^t)^V_{max}$. (*a–c*) The region defined by $Re_L > 100$ that encompasses the billows for cases 1, 5 and 8, respectively. The dashed line shows the approximate height of the upslope surge above the bottom, which is approximately equal to the incoming wave amplitude a. (*d*) $L_b^{max}/2a$ as a function of $k\delta$ for all cases. The vertical dotted line represents $k\delta$ regimes I and II defined in § 5.1. (*e*) $L_b^{max}/2a$ as a function of Fr_k^{max} for all cases.

supporting internal wave motion may change on daily or seasonal time scales. We began with a physical description of wave breaking as a function of $k\delta$. The breaking process is similar for all cases, and agrees with the description in Arthur & Fringer (2014). A collapsing breaker leads to an upslope surge of dense fluid, during which turbulence is generated in regions of unstable stratification within billows at the interface and underneath the nose of the upslope surge.

The local irreversible mixing efficiency R_f^* was found to vary between 0 and 1 throughout the turbulent region of the flow. It was relatively large in the billow roll-up regions and at the nose of the upslope surge, where ϵ_p^t was elevated, and smaller within the billow cores and throughout the rest of the turbulent region. The bulk (spatially and time-averaged) R_f^* was found to be approximately 0.3 for each case, indicating little variation with the initial interface thickness $k\delta$. Using the parameter space of Mater & Venayagamoorthy (2014) and restricting the data to the Re_L and ST_L of maximum turbulent mixing, the mean irreversible flux Richardson number $\langle R_f^* \rangle_c$ was found to vary with the turbulent Froude number Fr_k for each case. However, the $\langle R_f^* \rangle_c$ versus Fr_k curves showed no clear dependence on $k\delta$. Their trends were captured by an overall mean irreversible flux Richardson number $\langle R_f^* \rangle_{all}$ that reached a local maximum of approximately 0.36 for $Fr_k \approx 0.7$, where the balance of turbulence and stratification leads to the optimal mixing efficiency.

Unlike the local turbulent mixing efficiency measures based on R_f^*, the volume-integrated turbulent mixing efficiency η_B^t was found to vary with $k\delta$, ranging from 0.25 for low $k\delta$ to a maximum of 0.37 for $k\delta \approx 1$. For $k\delta > 1$, $\eta_B^t \approx 0.35$. In order to explain the variation in η_B^t with $k\delta$ based on the state of turbulence during wave breaking, we showed that Fr_k^{max}, the Froude number at which the maximum turbulent mixing occurs over the course of a breaking event, can be used to predict η_B^t, which is maximized for $Fr_k^{max} \approx 0.4$. Physically, we found that Fr_k^{max} is controlled by the vertical length scale of billows at the interface during wave breaking.

We note that our findings are limited by the chosen parameter space, wherein the interface thickness $k\delta$ was varied, but the wave steepness ka and the bathymetric slope s remained constant. Previous studies (Boegman *et al.* 2005; Venayagamoorthy & Fringer 2007; Aghsaee *et al.* 2010; Arthur & Fringer 2014) have shown that wave breaking dynamics and energetics change with wave amplitude and bathymetric slope. Additionally, due to computational restrictions, we have limited our results to $Pr = 1$ and a relatively low wave Reynolds number $Re_w \approx 150$, which are not realistic in a geophysical sense. Future work on turbulence and mixing in breaking internal waves on slopes should address these limitations by exploring a wider parameter space.

Acknowledgements

R.S.A. gratefully acknowledges the support of the Stanford Graduate Fellowship (SGF). R.S.A. and O.B.F. gratefully acknowledge the support of ONR grant N00014-08-1-0904 (scientific officers Dr C. L. Vincent, Dr T. Paluszkiewicz and Dr S. Harper). We gratefully acknowledge the US Army Research Laboratory DoD Supercomputing Resource Center for computer time on Pershing and Excalibur and especially thank the diligent staff at the HPC Help Desk for their support. We also thank O. Murray of ONR for ensuring our access to these resources. Finally, we thank K. S. Nelson for helpful discussions, and three anonymous referees for their thoughtful reviews of the manuscript.

REFERENCES

AGHSAEE, P., BOEGMAN, L. & LAMB, K. G. 2010 Breaking of shoaling internal solitary waves. *J. Fluid Mech.* **659**, 289–317.

ARTHUR, R. S. 2015 Numerical investigation of breaking internal waves on slopes: dynamics, energetics, and transport. PhD thesis, Stanford University.

ARTHUR, R. S. & FRINGER, O. B. 2014 The dynamics of breaking internal solitary waves on slopes. *J. Fluid Mech.* **761**, 360–398.

ARTHUR, R. S. & FRINGER, O. B. 2016 Transport by breaking internal gravity waves on slopes. *J. Fluid Mech.* **789**, 93–126.

BLUTEAU, C. E., JONES, N. L. & IVEY, G. N. 2013 Turbulent mixing efficiency at an energetic ocean site. *J. Geophys. Res.* **118** (9), 4662–4672.

BOEGMAN, L., IVEY, G. N. & IMBERGER, J. 2005 The degeneration of internal waves in lakes with sloping topography. *Limnol. Oceanogr.* **50** (5), 1620–1637.

BOGUCKI, D., DICKEY, T. & REDEKOPP, L. G. 1997 Sediment resuspension and mixing by resonantly generated internal solitary waves. *J. Phys. Oceanogr.* **27** (7), 1181–1196.

CARTER, G. S., GREGG, M. C. & LIEN, R. 2005 Internal waves, solitary-like waves, and mixing on the Monterey Bay shelf. *Cont. Shelf Res.* **25** (12), 1499–1520.

CHOU, Y. J. & FRINGER, O. B. 2010 A model for the simulation of coupled flow-bed form evolution in turbulent flows. *J. Geophys. Res.* **115**, C10041.

CUI, A. 1999 On the parallel computation of turbulent rotating stratified flows. PhD thesis, Stanford University.

DAVIS, K. A. & MONISMITH, S. G. 2011 The modification of bottom boundary layer turbulence and mixing by internal waves shoaling on a barrier reef. *J. Phys. Oceanogr.* **41** (11), 2223–2241.

DÖRNBRACK, A. 1998 Turbulent mixing by breaking gravity waves. *J. Fluid Mech.* **375**, 113–141.

DUNCKLEY, J. F., KOSEFF, J. R., STEINBUCK, J. V., MONISMITH, S. G. & GENIN, A. 2012 Comparison of mixing efficiency and vertical diffusivity models from temperature microstructure. *J. Geophys. Res.* **117**, C10.

FERZIGER, J. H. & PERIĆ, M. 2002 Solution of the Navier–Stokes equations. In *Computational Methods for Fluid Dynamics*, pp. 157–216. Springer.

FRINGER, O. B. & STREET, R. L. 2003 The dynamics of breaking progressive interfacial waves. *J. Fluid Mech.* **494**, 319–353.

GARGETT, A. E. & MOUM, J. N. 1995 Mixing efficiencies in turbulent tidal fronts: results from direct and indirect measurements of density flux. *J. Phys. Oceanogr.* **25** (11), 2583–2608.

HÄRTEL, C., CARLSSON, F. & THUNBLOM, M. 2000 Analysis and direct numerical simulation of the flow at a gravity-current head. Part 2. The lobe-and-cleft instability. *J. Fluid Mech.* **418**, 213–229.

HOSEGOOD, P., BONNIN, J. & VAN HAREN, H. 2004 Solibore-induced sediment resuspension in the Faeroe-Shetland channel. *Geophys. Res. Lett.* **31**, L09301.

HOSEGOOD, P. & VAN HAREN, H. 2004 Near-bed solibores over the continental slope in the Faeroe-Shetland channel. *Deep-Sea Res.* II **51** (25), 2943–2971.

HULT, E. L., TROY, C. D. & KOSEFF, J. R. 2011 The mixing efficiency of interfacial waves breaking at a ridge: 2. Local mixing processes. *J. Geophys. Res.* **116**, C02004.

IVEY, G. N. & IMBERGER, J. 1991 On the nature of turbulence in a stratified fluid. Part i: the energetics of mixing. *J. Phys. Oceanogr.* **21** (5), 650–658.

IVEY, G. N., WINTERS, K. B. & KOSEFF, J. R. 2008 Density stratification, turbulence, but how much mixing? *Annu. Rev. Fluid Mech.* **40** (1), 169–184.

KLYMAK, J. M. & MOUM, J. N. 2003 Internal solitary waves of elevation advancing on a shoaling shelf. *Geophys. Res. Lett.* **30** (20), 2045.

LAMB, K. G. 2002 A numerical investigation of solitary internal waves with trapped cores formed via shoaling. *J. Fluid Mech.* **451**, 109–144.

LAMB, K. G. 2014 Internal wave breaking and dissipation mechanisms on the continental slope/shelf. *Annu. Rev. Fluid Mech.* **46**, 231–254.

LEICHTER, J. J., WING, S. R., MILLER, S. L. & DENNY, M. W. 1996 Pulsed delivery of subthermocline water to Conch Reef (Florida Keys) by internal tidal bores. *Limnol. Oceanogr.* **41** (7), 1490–1501.

LEONARD, B. P. 1979 A stable and accurate convective modelling procedure based on quadratic upstream interpolation. *Comput. Meth. Appl. Mech. Engng* **19** (1), 59–98.

LIN, C. L., FERZIGER, J. H., KOSEFF, J. R. & MONISMITH, S. G. 1993 Simulation and stability of two-dimensional internal gravity waves in a stratified shear flow. *Dyn. Atmos. Oceans* **19** (1), 325–366.

LINDEN, P. F. & REDONDO, J. M. 1991 Molecular mixing in Rayleigh–Taylor instability. Part i: global mixing. *Phys. Fluids* A **3** (5), 1269–1277.

LOZOVATSKY, I. D. & FERNANDO, H. J. S. 2013 Mixing efficiency in natural flows. *Phil. Trans. R. Soc. Lond.* A **371**, 20120213.

MATER, B. D. & VENAYAGAMOORTHY, S. K. 2014 The quest for an unambiguous parameterization of mixing efficiency in stably stratified geophysical flows. *Geophys. Res. Lett.* **41** (13), 4646–4653.

MCEWAN, A. D. 1983*a* Internal mixing in stratified fluids. *J. Fluid Mech.* **128**, 59–80.

MCEWAN, A. D. 1983*b* The kinematics of stratified mixing through internal wave breaking. *J. Fluid Mech.* **128**, 47–57.

MICHALLET, H. & IVEY, G. N. 1999 Experiments on mixing due to internal solitary waves breaking on uniform slopes. *J. Geophys. Res.* **104** (C6), 13467–13477.

MOORE, C. D., KOSEFF, J. R. & HULT, E. L. 2016 Characteristics of bolus formation and propagation from breaking internal waves on shelf slopes. *J. Fluid Mech.* **791**, 260–283.

MOUM, J. N. 1996 Efficiency of mixing in the main thermocline. *J. Geophys. Res.* **101** (C5), 12057–12069.

MUNK, W. & WUNSCH, C. 1998 Abyssal recipes ii: energetics of tidal and wind mixing. *Deep-Sea Res.* **45** (12), 1977–2010.

OAKEY, N. S. 1982 Determination of the rate of dissipation of turbulent energy from simultaneous temperature and velocity shear microstructure measurements. *J. Phys. Oceanogr.* **12** (3), 256–271.

OMAND, M. M., LEICHTER, J. J., FRANKS, P. J., GUZA, R. T., LUCAS, A. J. & FEDDERSEN, F. 2011 Physical and biological processes underlying the sudden appearance of a red-tide surface patch in the nearshore. *Limnol. Oceanogr.* **56** (3), 787–801.

OSBORN, T. R. 1980 Estimates of the local rate of vertical diffusion from dissipation measurements. *J. Phys. Oceanogr.* **10** (1), 83–89.

OSBORN, T. R. & COX, C. S. 1972 Oceanic fine structure. *Geophys. Fluid Dyn.* **3** (1), 321–345.

PELTIER, W. R. & CAULFIELD, C. P. 2003 Mixing efficiency in stratified shear flows. *Annu. Rev. Fluid Mech.* **35** (1), 135–167.

PINEDA, J. 1994 Internal tidal bores in the nearshore: warm-water fronts, seaward gravity currents and the onshore transport of neustonic larvae. *J. Mar. Res.* **52** (3), 427–458.

QUARESMA, L. S., VITORINO, J., OLIVEIRA, A. & DA SILVA, J. 2007 Evidence of sediment resuspension by nonlinear internal waves on the western Portuguese mid-shelf. *Mar. Geol.* **246** (2), 123–143.

REHMANN, C. R. & KOSEFF, J. R. 2004 Mean potential energy change in stratified grid turbulence. *Dyn. Atmos. Oceans* **37** (4), 271–294.

SCOTTI, A. & WHITE, B. 2014 Diagnosing mixing in stratified turbulent flows with a locally defined available potential energy. *J. Fluid Mech.* **740**, 114–135.

SEIM, H. E. & GREGG, M. C. 1995 Energetics of a naturally occurring shear instability. *J. Geophys. Res.* **100** (C3), 4943–4958.

SHIH, L. H. 2003 Numerical simulations of stably stratified turbulent flow. PhD thesis, Stanford University.

SHIH, L. H., KOSEFF, J. R., IVEY, G. N. & FERZIGER, J. H. 2005 Parameterization of turbulent fluxes and scales using homogeneous sheared stably stratified turbulence simulations. *J. Fluid Mech.* **525**, 193–214.

SIMPSON, J. E. 1972 Effects of the lower boundary on the head of a gravity current. *J. Fluid Mech.* **53** (4), 759–768.

SLINN, D. N. & RILEY, J. J. 1998 Turbulent dynamics of a critically reflecting internal gravity wave. *Theor. Comput. Fluid Dyn.* **11** (3–4), 281–303.

SMYTH, W. D., MOUM, J. N. & CALDWELL, D. R. 2001 The efficiency of mixing in turbulent patches: inferences from direct simulations and microstructure observations. *J. Phys. Oceanogr.* **31** (8), 1969–1992.

TROY, C. D. & KOSEFF, J. R. 2005 The instability and breaking of long internal waves. *J. Fluid Mech.* **543**, 107–136.

VENAYAGAMOORTHY, S. K. & FRINGER, O. B. 2007 On the formation and propagation of nonlinear internal boluses across a shelf break. *J. Fluid Mech.* **577**, 137–159.

VENAYAGAMOORTHY, S. K. & KOSEFF, J. R. 2016 On the flux Richardson number in stably stratified turbulence. *J. Fluid Mech.* **798**, R1.

WALTER, R. K., SQUIBB, M. E., WOODSON, C. B., KOSEFF, J. R. & MONISMITH, S. G. 2014*a* Stratified turbulence in the nearshore coastal ocean: dynamics and evolution in the presence of internal bores. *J. Geophys. Res.* **119** (12), 8709–8730.

WALTER, R. K., WOODSON, C. B., ARTHUR, R. S., FRINGER, O. B. & MONISMITH, S. G. 2012 Nearshore internal bores and turbulent mixing in southern Monterey Bay. *J. Geophys. Res.* **117**, C07017.

WALTER, R. K., WOODSON, C. B., LEARY, P. R. & MONISMITH, S. G. 2014*b* Connecting wind-driven upwelling and offshore stratification to nearshore internal bores and oxygen variability. *J. Geophys. Res.* **116** (6), 3517–3534.

WINTERS, K. B., LOMBARD, P. N., RILEY, J. J. & D'ASARO, E. A. 1995 Available potential energy and mixing in density-stratified fluids. *J. Fluid Mech.* **289**, 115–128.

WUNSCH, C. & FERRARI, R. 2004 Vertical mixing, energy, and the general circulation of the oceans. *Annu. Rev. Fluid Mech.* **36**, 281–314.

YAMAZAKI, H. & OSBORN, T. R. 1993 Direct estimation of heat flux in a seasonal thermocline. *J. Phys. Oceanogr.* **23** (3), 503–516.

ZANG, Y., STREET, R. L. & KOSEFF, J. R. 1994 A non-staggered grid, fractional step method for time-dependent incompressible Navier–Stokes equations in curvilinear coordinates. *J. Comput. Phys.* **114**, 18–33.